Finding the Optimal Unsaturated Zone Storage Change Estimation Method to Improve Water Accounting in Vietnam

Gracia Plenita Agnindhira

T̃U Delft

Finding the Optimal Unsaturated Zone Storage Change Estimation Method to Improve Moisture Accounting in Vietnam

A case study of the Ca and the Downstream Red River Basin in Vietnam

by

G. P. Agnindhira

to obtain the degree of Master of Science
at the Delft University of Technology,
to be defended publicly on Friday October 28, 2016 at 4 pm.

TUDelft

Abstract

Water Accounting Plus or WA+ was developed as an answer to the ever growing need of a reliable, basin-scale, moisture accounting. The main attraction of WA+ is its ability to draw an explicit relationship between water users and available water resources. By doing this, it is able to improve the understanding of human and nature interactions in the field of water resource management. Similar to other moisture accounting methods, the computation in WA+ starts with the tracking of various hydrological stocks that are present in the area of interest. The accuracy and reliability of these inputs will significantly influence the performance of WA+. The terrestrial storage change or ΔS is one of those required inputs. The term itself is a combination of a surface component (ΔS_{SW}), a groundwater component (ΔS_{GW}), and an unsaturated zone component (ΔS_{UZ}).

Since it is very complicated to directly measure ΔS_{UZ}, many moisture accountings implement a certain estimation method to get an approximation of the real value. Among the more popular ΔS estimation methods are hydrological models (i.e. WaterPix, STREAM, and PCRGlobwb) and land surface model (i.e. GLDAS-Noah). In addition to these, there are also empirical relationships that are used to derive the unsaturated zone soil moisture from the surface condition. A more uncommon method is to use the Budyko Curve approach on to solve an unsteady water balance. This thesis aims to find the optimal (ΔS_{UZ}) estimation method for the application within WA+. The Ca River Basin and the Downstream Red River Basin were chosen as the study areas. A period of 4 years, from December 2006 to 2010 was chosen as the simulation period. Each method was run on a monthly time step to facilitate the need of a monthly application of WA+.

The methods mentioned above were evaluated based on their ability to regenerate the observed streamflow at available measuring stations in both basins. An additional check was also done by comparing the estimated ΔS_{UZ} from each method to the streamflow-derived ΔS_{UZ}. A second evaluation, based on the spatial distribution of land use and land cover classes, was done to see which of the methods is able to reflect the variation of ΔS_{UZ} based on the land use and land cover types. The results of both evaluation processes suggest that the downscaled products of the PCRGlobwb model are the most accurate method to estimate ΔS_{UZ}. However, it is not the most practical since the original spatial resolution of the outcomes of this model is relatively coarse (i.e. 10 km) which will be a problem if the study area is classified as a small to medium basin.

On the other hand, although the statistical performance of the WaterPix model and the empirical relationship are quite low during the evaluation process, these two methods show promising potential for application within WA+, considering their flexible computing structure and their ability to produce outcomes at a fine spatial resolution (i.e. 250m). Further investigation should test the accuracy of these methods in regions with other hydrological characteristics. Using the same evaluation processes, the results from the Budyko Curve method are found to be the least accurate.

G. P. Agnindhira
Delft, October 2016

Acknowledgement

Contents

List of Figures

List of Tables

Glossary

ΔS Storage change.

ASCAT Advanced Scatterometer.

CHIRPS Climate Hazards Group Infra-Red Precipitation Station.

DEM Digital Elevation Model.

eMODIS EROS Moderate Resolution Imaging Spectroradiometer.

ERA ECMWF re-analysis project.

EROS Earth Resources Observations and Sciences.

ET The combination of Evaporation and Transpiration.

FAO Food and Agriculture Organization of the United Nations.

GLCC Global Land Cover Characterization.

GLDAS Global Land Data Assimilation System.

GSFC Goddard Space Flight Center.

GTOPO30 Global 30-Arc Second Elevation.

HWSD Harmonized World Soil Database.

IGBP International Geosphere-Biosphere Programme.

IWMI International Water Mangement Institute.

LAI Leaf Area Index.

LSM Land Surface Model.

LST Local Sidereal Time.

MODIS Moderate Resolution Imaging Spectroradiometer.

NASA National Aeronautics and Space Administration.

NCEP National Centers for Environmental Prediction.

NDVI Normalized Difference Vegetation Index.

NOAA National Oceanic and Atmospheric Administration.

P Precipitation.

PCRGlobwb PCRaster Global Water Balance.

Q Surface runoff.

SCS-CN Soil Conservation Services Curve Number.

SEBAL Surface Energy Balance Algorithm for Land.

STATSGO The Digital General Soil Map of the United States.

STREAM Spatial Tools for River basins and Environment and Analysis of Management options.

TRMM Tropical Rainfall Measurement Mission.

UN SEEAW United Nations System of Environmental-Economic Accounting for Water.

USGS United States Geological Survey.

WA+ Water Accounting Plus.

1

Introduction

The global sustainable development movement has put the need of responsible water resources exploitation as its utmost priority. In order to answer this challenge responsibly, a clear understanding of the governing hydrological processes and their interactions with different groups of user is required. However, this task proved to be difficult since there is a lack of coherency in the terminologies and data sharing among many different water resource management institutions. The up and running WA+ framework was proposed as an answer to the issue mentioned above.

1.1. Background

The distinctive quality of WA+ lies in its ability to draw an explicit relationship between the available water resources and the water users, while other water accounting methods (i.e. IWMI Water Accounting, FAO Aquastat, UN SEEAW, the Australian Water Accounting, etc.) do not manage to achieve this [12, 27, 43]. WA+ is also a depletion based accounting method, therefore it is able to avoid the problem of withdrawals data scarcity and the errors that usually come with neglecting the return flows and the partitioning of ET [27].

In short, the WA+ framework provides a coherent and consistent method to track the quantity of fluxes and stocks in the hydrological cycle. Further, the outcome of WA+ may be utilized as a foundation for a constructive discussion about the partitioning of water resources among the users. The WA+ framework uses a mass balance approach where the outflow from a certain area of interest (e.g. country, basin, etc.) is explicitly related to the net inflow and the depletions. Eq. 1.1 and Figure 1.1 show the mass balance equation of WA+ and its graphical visualization respectively.

$$P - ET_{total} + Q_{in} - Q_{out} = \Delta S \tag{1.1}$$

The combination of P, Q_{in}, and ΔS forms the net inflow into the area of interest. The net inflow represents the available water that can be converted into two components: the combination of evaporation and transpiration from the landscape (ET_{prec}) and exploitable water. ET_{prec} is also known as the Green Water since its supply comes solely from precipitation that falls across the area. Although the Green Water only accounts for natural water extraction, the influence of human actions on ET_{prec} may occur through conversion of land use and vegetation density. The exploitable water represents the portion of water that is available for downstream use after ET_{prec} occurs. Conceptually, the exploitable water is analogous to the Blue Water. In the end, the depletion of water is quantified as the combination of total ET (i.e. ET_{prec} and ET_q) and flow from the area of interest to the sinks [27].

A reliable and accurate quantification of ΔS can improve WA+ effectiveness in many different ways. Firstly, while multi annual or annual WA+ framework analysis can assume that ΔS is negligible, shorter time step (e.g. monthly) water balance analysis is proven to be sensitive to ΔS [42]. In most cases, especially in the field of agriculture, a short time step moisture accounting is more desirable than annual accounting because it provides information on the intra-annual variability of water storage which is critical for the planning of cropping strategy (e.g water distribution among irrigation schemes, etc.).

Secondly, in regions with pronounced seasonality, an accurate estimation of ΔS might provide the right explanation on how crops can sustain the drought periods and at the same time helps to improve the identification of the Blue and Green water resources. In the most practical way, an accurate estimation of ΔS
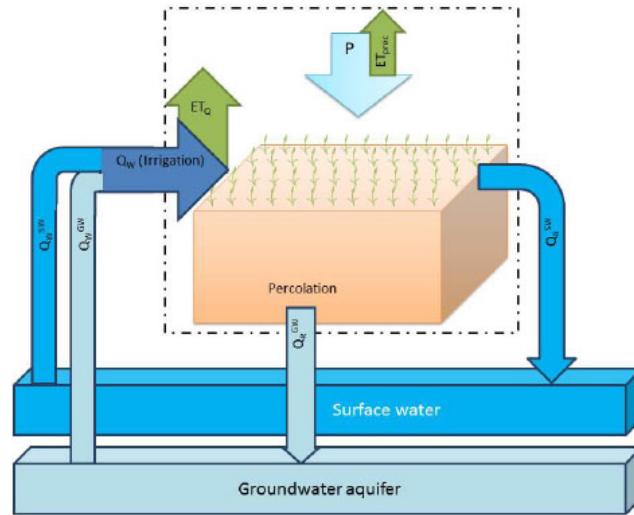
Figure 1.1: Graphical visualization of WA+ water balance

combined with enough information on water users will enable water managers to determine which users produce water and which ones use more water that what is allocated to them. In addition, ΔS is also effective in identifying the extent of dependency of a certain ecosystem to its water storages [27, 42].

ΔS itself is actually a bulk term which consists of a groundwater component, a surface component, and an unsaturated zone component. This study only focuses on the latter, since the rooting system of most vegetation is located in this particular zone. It also acts as a critical factor in controlling the land-atmospheric moisture exchange, the hydrological responses, and the bio-geochemical processes [20, 52].

Recent research by de Boer-Euser et al. [9] suggested that the capacity of the storage is largely influenced by the climatic condition rather than other factors. Vegetation tends to invest their resources efficiently, especially during the drought period or the periods between rainfall events. This tendency is physically translated into the size of the storage in the soil where the rooting system is located. Acknowledging the dependency between the climatic condition and the size of storage in the unsaturated zone, it is no longer accepted to neglect ΔS in a water balance equation, especially if it is applied in a short time scale analysis. The estimation of ΔS in the unsaturated zone should also be done in a spatially distributed manner since the difference in both land use and climatic conditions will result in the spatial variability of water storage capacity in the unsaturated zone. More importantly, the right method should be able to produce independent estimates of ΔS so that the application within the current WA+ framework will not introduce an additional bias.

In conclusion, the amount of ΔS in the unsaturated zone is influenced by the variability of the climatic condition and the type of land use and land cover. Since both variables are functions of space and time, an acceptable ΔS estimation method should consider a high temporal and spatial variability.

1.2. Research Objective and Questions
Considering the presence of various ΔS estimation methods and the importance of applying an accurate estimation of the unsaturated zone ΔS in the WA+ framework, this master thesis aims to provide the answer to that challenge. Spatial variability of ΔS in the unsaturated zone will be observed in monthly basis in order to facilitate the need of monthly WA+ application. Therefore, the main objective of this work is:

To determine the optimal method to estimate spatially distributed monthly ΔS in the unsaturated zone using remote sensing data and the information on land use practices in the area which further will improve the reliability and accuracy of the WA+ framework.

In order to evaluate different estimation methods, two study areas and a period of observation was established. The Ca Basin and the lower part of the Red River Basin in Vietnam were selected as the study areas based on the presence of abundant land use and land cover information and the streamflow measurement from previous studies done in both areas [36, 42]. Taking in to account the inter-annual climatic variability

and the availability of the hydrological data, a period of 4 years (from December 2006 to December 2010) was chosen as the simulation and the observation period.

Constrained within the study areas and the period of observation, the main objective of the research is translated in to several research questions:

1. Given the case study small to medium basins' sizes, is the global distributed hydrological model (PCR-Globwb) a better option to simulate monthly unsaturated zone ΔS compared to the global land-surface model (GLDAS-Noah)?

2. Can a model-independent, empirical method, using top soil moisture information and vegetation indices from remote sensing, outperform the more popular global hydrological or land-surface models?

3. Can a curve number based distributed hydrological model (i.e. WaterPix) produce a reliable estimation of the monthly unsaturated zone ΔS in small to medium basins?

4. Does the soil moisture deficit derived from the Budyko Curve accurately represent the ΔS in the unsaturated zone in small to medium basins?

2

Materials and Methods

In order to achieve the research objective, this study follows a certain research methodology as shown in Figure 2.1. It starts with a literature study to get the bigger and more complete picture about the previous studies that have been done in the estimation of unsaturated zone ΔS (e.g. the most common methods to calculate ΔS, etc.). Once the general ideas of the available methods are known, the next step is to gather the required input to perform the calculation or the simulation on the study areas. This ranges from directly extracting the datasets from public online data portals or cooperating with the corresponding institutions to get their limited access.
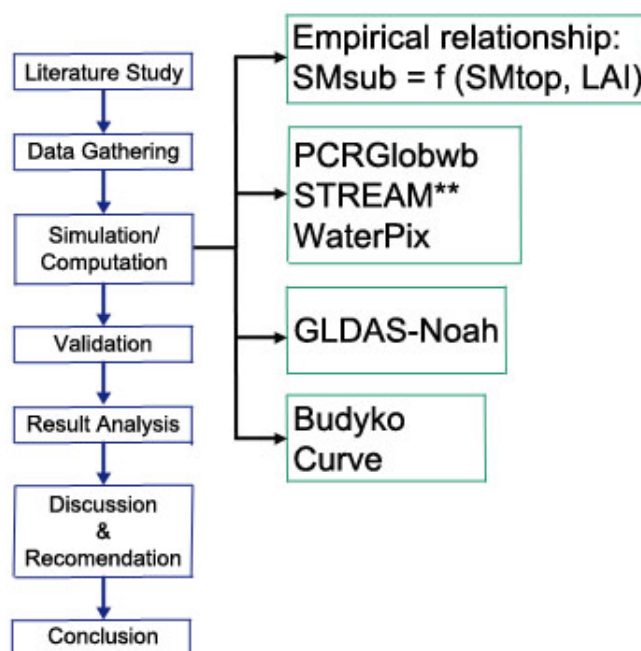
Figure 2.1: The research methodology

The estimation methods in this study are derived from 4 different branches; a-model-independent empirical relationship between the ground surface and the unsaturated zone, hydrological models, land surface models, and the Budyko Curve approach. Once the results from each method are attained, a validation is due. This study takes 2 different aspects into account to determine which of the methods is most suitable for WA+.

More detailed explanation of each estimation method and the validation process is provided in the sections below.

2.1. Empirical Relationship Between the Ground Surface and the Unsaturated Zone

The main idea behind this method is to make use of the top soil moisture storage and the maximum rooting depth ability to indicate the amount of moisture storage in the unsaturated zone.

The amount of water in the top soil layer affects the variability in the unsaturated zone water content at all time. However, in monthly basis, the greenness of vegetation cover also reflects the availability of soil water for extraction by the vegetation roots. The degree of saturation in the unsaturated zone is assumed to exceed the degree of saturation in the top soil when vegetation is actively performing photosynthetic processes. Under the presence of no vegetation cover, the unsaturated zone soil moisture is directly connected to the top soil moisture. An empirical formula derived from this relationship is applied in the ETLook model v.01 [6], which then adopted in this study. The empirical formula is shown in Eq. 2.1.

$$SE_{sub} = 0.1\,(LAI) + (1 - 0.1\,(LAI))\left[1 - \exp\left(SE_{top}\,(-0.5\,(LAI) - 1)\right)\right] \tag{2.1}$$

SE_{top} represents the effective saturation in the top soil layer which was calculated by multiplying the relative top soil moisture from ASCAT (%) with the soil porosity from HWSD (m^3/m^3). The ASCAT products are available in daily time step as a-5 days mean for both ascending and descending overpasses [16, 34, 35, 49]. The descending overpass is taken at 09.30 LST and the ascending is taken at 21.30 LST on the same day. Generally, over the study areas, the descending overpasses have better quality compared to the ascending overpasses. This study used the combination of both overpasses, excluding data with poor quality.

LAI is commonly accepted as the proxy of canopy light absorption. In this study, LAI is used to represent the vegetation greenness or the leaf water. However, LAI cannot be measured directly by satellite sensors [21]. This study adopted the approach embedded in the SEBAL model which calculates the value of LAI from Vegetation Cover (VC) that is derived from NDVI data as shown in Eq. 2.2 [5]. NDVI is the widely accepted indicator of the vegetation's biophysical activity, since it is able to represent the distribution of vegetation cover over the ground surface. A time series of NDVI data shows the variability of vegetation's state in its period of growth. Higher NDVI values correspond to denser vegetation (e.g. tropical rainforest, etc.) while lower NDVI values usually represent bare soil and sparsely vegetated area. In this study, 0.8 was used as the maximum NDVI boundary condition to represent full vegetation cover and 0.125 as the minimum NDVI boundary condition to represent bare soil. The NDVI products used in this study is the eMODIS NDVI, provided from the Moderate Resolution Imaging Spectroradiometer (MODIS) data acquired by the National Aeronautics and Space Administration's (NASA) Earth Observing System. The NDVI dataset for Vietnam was retrieved from Earth Explorer, courtesy of the U.S. Geological Survey [26].

$$VC = 1 - \left(\frac{0.8 - NDVI}{0.8 - 0.125}\right)^{0.7} \tag{2.2}$$

$$LAI_1 = \frac{log\,(-(VC - 1))}{-0.45} \tag{2.3}$$
$$LAI_2 = 9.519\,(NDVI)^3 + 0.104\,(NDVI)^2 + 1.236\,(NDVI) - 0.257$$

The SEBAL model applies 4 different ways to calculate LAI however, this study only uses 2 out of the 4 ways to calculate LAI and took the average of both calculations as the final LAI value. The first equation in Eq. 2.3 is based on the asymptotic relationship between LAI and VC, where a is the coefficient of light extinction with a range of 0.4 to 0.65. This study treated a as a constant parameter with a value of 0.45 since vegetation type based variability of a is not available yet. In order to balance this simplification, a second LAI function is needed. Using an empirical approach, the second equation in Eq. 2.3 calculates LAI as a function of NDVI.

In order to get the actual water content in the unsaturated zone, SE_{sub} or saturation degree in the unsaturated zone from Eq. 2.1 (m^3/m^3) was then adjusted to the saturated water content (m^3/m^3) and residual water content (m^3/m^3). Both of these soil parameters are available in a spatially distributed manner at 1 km resolution as parts of HiHydroSoil soil map courtesy of FutureWater.

The other variable needed to complete this method is the rooting depth of the vegetation cover. The rooting depth was derived from the maximum root zone storage capacity ($S_{R,max}$) developed by Wang-Erlandsson et al. [52]. Her study assumes that vegetation adjusts its rooting system to bridge drought periods. Hence, the size of storage capacity in the unsaturated zone is optimized based on the moisture demands and the nutrient resources consumption by vegetation during drought periods.

The Wang-Erlandsson $S_{R,max}$ product is available at 50 km spatial resolution while the available water content that was retrieved from the FutureWater's HiHydroSoil dataset is available at 1 km spatial resolution. The unit of the $S_{R,max}$ product mm and the unit of the available water content is m^3/m^3. A downscaling process was performed to the $S_{R,max}$ map so that both datasets have the same spatial resolution (i.e. 250 m). A monthly average of NDVI over the whole period of observation was calculated and used as proxy of the downscaling process. The use of NDVI as a proxy is based on its correlation with the extent of vegetation rooting depth in certain conditions. The downscaling process was adopted from the study performed by Immerzeel et al. [25]. Detailed steps of the downscaling process are explained in section 2.6: Downscaling Process at the end of this chapter.

Once the Wang-Erlandsson $S_{R,max}$ has the appropriate spatial resolution (i.e. 250 m), the rooting depth (mm) was calculated by dividing Wang-Erlandsson $S_{R,max}$ with the total available water content in the soil. Since $S_{R,max}$ is analytically the maximum storage capacity, the rooting depth derived from this variable should be seen as the upper boundary for rooting depth instead of the actual rooting depth itself.

The amount of soil moisture in the unsaturated zone (mm) is calculated by multiplying the actual water content in the unsaturated zone (m^3/m^3) with the maximum rooting depth (mm). The overview of this method is shown in Figure 2.2 below.
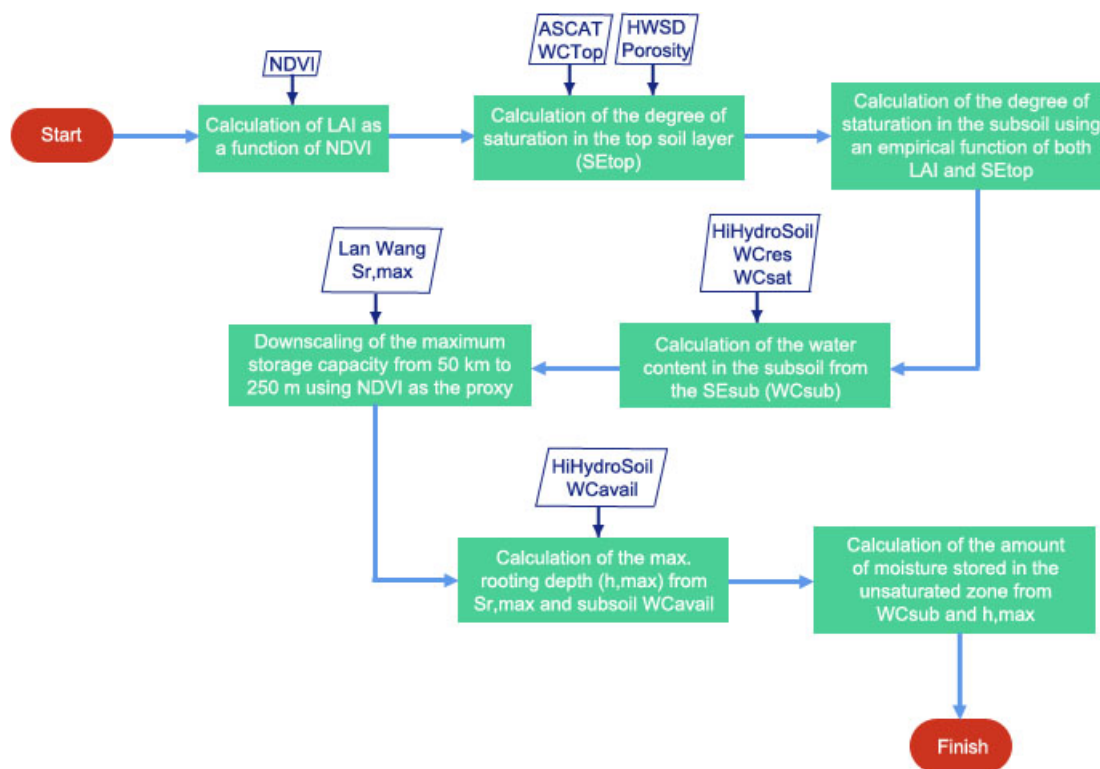
Figure 2.2: Flowchart of the empirical relationship of Method 1

Once the unsaturated zone water storage on every first day of the month is calculated, the ΔS is obtained by subtracting the magnitude of the storage in the next month from the current month. The unit of ΔS derived from this method is millimetre.

2.2. Hydrological Models

Hydrological models are frequently used to simulate streamflow in large basins. These models use a water balance approach to correctly simulate and rout surface runoff into the basin outlets. Generally, hydrological models can be divided in to two different categories; lumped and distributed models. The models from each category can be further differentiated into empirical models, conceptual based models, and process based models. This study adopts two different approaches under the distributed model category. The first is semi-empirical distributed models and the second is conceptual distributed models.

Empirical models are often said as the most robust approach towards streamflow generation because these models simply use an empirical relationship between the hydrological influx and the streamflow to simulate the streamflow generation itself. On the other hand, the conceptual models have a more elegant approach towards the streamflow generation. These models are built based on the conceptualization of the dominant physical processes that contribute to the generation of streamflow. The processes are explained using mathematical equations and reservoirs are used to represent the hydrological stocks, where the water balance equation in each reservoir must be closed. The application of distributed modelling on top of both empirical and conceptual models allows the users to preserve the impact of distributed input (i.e. precipitation, total evaporation and transpiration, elevation, land use and land cover, etc.) and translate it into the generation of streamflow [40].

Three hydrological models were used in this study as examples of two different modelling approaches explained above, the WaterPix model as an example of a semi-empirical distributed model and the STREAM and the PCRGlobwb model as examples of conceptual distributed models. It should be noted that although both STREAM and PCRGlobwb are distributed and conceptual based, they have some fundamental differences. The most significant aspect is the fact that PCRGlobwb was developed as a global hydrological model while STREAM is meant for a smaller, more local, spatial scale analysis. Hence, the model structure and the parameterization differ significantly. PCRGlobwb applies a more complex model parameterization while STREAM has a more modest and flexible structure. More detailed explanation on the background of each model is provided in the sub-sections below.

2.2.1. WaterPix

WaterPix is a name given to this semi-empirical distributed model which is based on the modified SCS-CN method. This study used an earlier version of the WaterPix model that was developed by Espinoza-Dávalos and Bastiaanssen [15]. SCS-CN method is a simple and robust way to calculate surface runoff based on the empirical relationship between precipitation and surface runoff itself [31]. The mathematical equation of the original SCS-CN method is shown in Eq. 2.4.

$$Q = \frac{(P - I_a)^2}{(P - I_a) + S}$$
$$I_a = 0.2S$$
$$S = \left(24.5 \times \frac{1000}{CN}\right) - 10$$

(2.4)

The set of equations above show that the relationship between P and Q is influenced by I_a, S, and the curve number (CN) of the study area. I_a or the initial abstraction serves as a threshold for the occurrence of surface runoff (Q) after each rainfall event. Ideally, the value of I_a should represent the demands from interception and evaporation processes, the amount of water that is retained in the depression storages, and the amount of water that infiltrates the soil [11]. The value of this parameter can be estimated through an empirical relationship using the S parameter, as shown in the second equation in Eq. 2.4.

Not to be confused by the common use of S as a symbol for soil moisture storage capacity, the S parameter in this case represents the potential retention of water in the soil after surface runoff begins. The value of S is based on the CN of the study area. According to SCS-CN, the value of CN varies based on several physical aspects such as the type of soil according to Hydrologic Soil Groups, land cover types, land treatment, and hydrologic conditions.

Conceptually, the computing steps of WaterPix are shown in the sequence of equations (i.e Eq. 2.5 to Eq. 2.7) below. The main assumption of WaterPix is that the annual Q is equal to the difference between annual P and annual ET (i.e. Eq. 2.5). However, in a smaller time scale (i.e. monthly and daily), the change in soil water storage becomes a contributing flux to the surface runoff generation process (i.e. Eq. 2.6).

$$0 = P_{ann} - ET_{ann} - Q_{ann}$$
$$Q_{ann} = P_{ann} - ET_{ann}$$

(2.5)

$$\Delta S_{monthly} = P_{monthly} - ET_{monthly} - Q_{monthly}$$

(2.6)

$Q_{monthly}$ is calculated using the first equation in Eq. 2.4 from the original SCS-CN. However, instead of using CN values from a look-up table, WaterPix uses an optimization process to find the value of S as shown

in Eq. 2.7. The value of S parameter is optimized so that yearly accumulation of monthly Q is equal to the annual Q from Eq. 2.5.

$$S = \left| S_{top,max} - S_{top,actual} \right| z \tag{2.7}$$

$S_{top,max}$ is the maximum available water content in the top soil and the $S_{top,actual}$ is the actual water content. The value of the available water content in topsoil from HiHydroSoil map was used as $S_{top,max}$. The z parameter is a tuning parameter and it is analogous to the vegetation rooting depth. The rooting depth used in this method was taken from the rooting depth calculation in Section 2.1, where it is treated as a function of both maximum storage capacity in the soil and available water content in the root zone. $S_{top,actual}$ was calculated from precipitation, total evaporation and transpiration, interception, soil moisture vertical profile, and the ratio between fast generated surface runoff and a combination of fast and slow generated runoff. Once monthly Q is known, monthly ΔS can be back-calculated using the same P and ET input.

The outcomes of the WaterPix model are monthly surface runoff, base flow, ΔS, and infiltration zone. The unit of the outcomes are millimetre. The model needs 6 input variables and 2 spatially distributed parameters as described in Table A.1 in the Appendix section. In order for the model to produce stable and more reliable result, the simulation should be done for at least a period of 2 years.

2.2.2. STREAM

The STREAM model is a conceptual distributed hydrological model that solves a water balance equation on a certain gridded landscape. In most cases, the STREAM model proved to be an effective tool to perform analysis on the hydrological impact of both land use and climate change in a river basin [36]. A simplification of the water balance used in the STREAM model is pictured as one linear reservoir as shown in Figure 2.3 below.
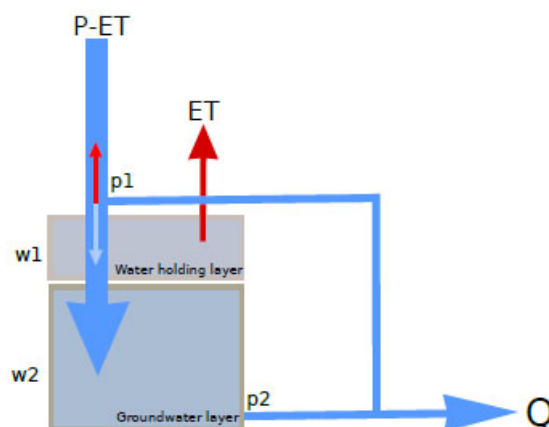
Figure 2.3: Simplification of the STREAM model structure

When $P - ET$ or the influx in a time step is positive, the resulting water is partitioned into two different components (i.e. the infiltrated and the surface component) based on the p_1 parameter. The surface component forms the majority of the fast flow surface runoff (Q) while the infiltrated component went further to the soil. The first layer of the soil is called the water holding layer. This layer will be filled with the infiltrated water until it reaches the saturation threshold. Only when this layer reaches saturation, then the infiltrated water can percolate further to the second soil layer which is treated as the groundwater reservoir. The p_2 parameter is used to calculate a fraction of the water in the groundwater reservoir that will contribute to the formation of base flow. The depth of each soil layer, w_1 and w_2, is treated as the other model parameters. If the influx at a time step is negative ($P < ET$), then water is taken from the water holding layer to balance out the demand and no surface runoff from the upper soil layer is produced [2, 24].

Since the STREAM model enables the incorporation of remote sensing data into a rainfall-runoff model, it can be used to perform simulation of water availability and river discharge in large river basins. The non-linearity character of these large basins is represented using a combination of threshold values and linear

reservoirs. The streamflow is generated by accumulating the surface runoff in the local drainage direction, using the information derived from a DEM layer. The STREAM model does not involved any surface runoff routing in its simulation since the surface runoff in each pixel is removed from the model within the same time step as it is generated [54]. This condition restricts the time step options that are allowed to be used in the simulation; it has to be at least as long as the residence time of water in the basin.

This study uses the STREAM model developed by Ate Poortinga for his study in the Ca River Basin [36]. The validation process using runoff data from several streamflow measuring stations in the Ca River Basin proved that his version of the STREAM model is able to generate a reliable simulation of monthly surface runoff with a spatial resolution of 250 m. Due to limited time and operating power, the STREAM model was only used to simulate the runoff in the Ca River Basin.

In order to run the model, the input should at least contain a DEM file and climate data. However, more information about the basin will increase the reliability of the simulation result. On the case of the Ca River Basin, the input datasets are shown in Table A.2 in the Appendix section.

The STREAM model produces three categories of spatially distributed outcomes; groundwater storage, soil water storage, and surface runoff. Based on the conceptual structure of STREAM itself, soil water storage was taken as the unsaturated zone moisture storage. The ΔS in unsaturated zone is calculated in millimetre as the difference between storage in the first day of the next month and the current month.

2.2.3. PCRGlobwb

PCRGlobwb model was developed as a tool to simulate global terrestrial hydrology in a grid-based manner using a leaky bucket approach [45]. The simplification of a vertical structure of the model is shown in Figure 2.4 below.
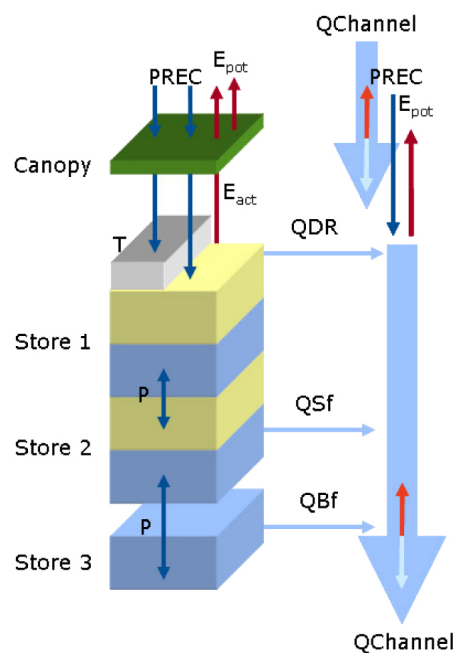
Figure 2.4: Simplification of the PCRGlobwb model structure

In each time step the model calculates the amount of water stored in two vertically stacked soil layers (Store 1 and Store 2) and in the underlying groundwater layer (Store 3) as a result of the vertical and lateral movement of water [46]. The first and the second soil layer are each treated as a finite reservoir with a maximum capacity of 0.3 m and 1.2 m respectively. On the other hand, the groundwater layer is modelled using an infinite reservoir.

The vertical water fluxes are comprised of downward and upward movement among the three underground layers and water exchange between top soil layer and atmosphere. The lateral water flux is equal to the total specific runoff which is a combination of interflow (i.e. flow of water through the preferential pathways in the unsaturated zone to the nearest water courses), groundwater flow (i.e. the base flow), and

overland flow.

The sub-grid spatial variability is built upon the land cover map from GLCC version 2 courtesy of the USGS EROS database and the separation between tall and short vegetation [45]. First, the GLCC land cover map is re-classified into four classes; open water, natural vegetation, rain fed crops, and irrigated crops. Second, a separation between tall and short vegetation is made for all vegetation classes with an addition of a bare soil fraction. The next step is to separate shallow open water from deep open water. This sub-grid classification is particularly useful where actual ET is involved in the simulation. However, the depth of the vegetation rooting system that is applied in the model computation is independent from these land cover classification.

The net input is made from a fraction of liquid precipitation that neither get intercepted by the canopy and evaporated, converted into snow pack (if the air temperature is below 0^oC), nor stored in the available pore space in the snow cover (if the air temperature is above 0^oC and there are already presence of snow). A fraction of the net input infiltrates the top soil layer and the rest is converted into overland flow. The partitioning of these fluxes is done based on the fraction of saturated soil contained in the top soil layer. If the saturation degree of the top soil layer is low, the net input will infiltrate fully to the soil layer and overland flow does not occur. The opposite will happen when the soil is partially or highly saturated [22].

The abstraction of water from soil layers is based on the magnitude of actual ET. These abstractions differ in mechanism according to the sub-grid spatial variability mentioned in the previous paragraph. Bare soil evaporation is limited by the amount of available water in the first soil layer after transpiration takes place. Short vegetation transpiration only involves extraction of water from the first soil layer while tall vegetation is able to extract water from both soil layers.

The vertical exchange between the first and the second soil layer is determined by the unsaturated hydraulic conductivity of each layer [46]. However, upward flux from the groundwater layer to the second soil layer has slightly different mechanism, where the capillary fringe occurrence is bounded by three conditions; field capacity of the second layer, the amount of water in the active groundwater storage, and the proximity of the water table. The hydraulic conductivity that drives this upward flux is the geometric mean of unsaturated hydraulic conductivity of the second soil layer and saturated hydraulic conductivity of the groundwater layer. Percolation from the second soil layer to the groundwater layer applies the same mechanism as the downward movement from the first soil layer to the second soil layer.

Interflow originates from the second soil layer. This lateral movement of water usually occurs in regions with presence of bedrock and steep hillslopes [45]. Neglecting interflow will result in the overestimation of groundwater storage and groundwater response time. PCRGlobwb takes a simplified approach to model this flux where the process is only activated when water content in the second soil layer reached field capacity.

Although the groundwater layer is assumed to be an infinite reservoir, it is further divided in to active and inactive storage. The active storage is where the generation of base flow takes place. PCRGlobwb uses a first order linear reservoir to model base flow with groundwater residence time as the calibrated parameter.

The total specific runoff of every cell is accumulated and routed over the drainage network that defines the flow from 8 cardinal directions. The routing method is done using a numerical solution of the Saint-Venant kinematic wave equation with a time explicit scheme and a variable time stepping [46]. The essential part of this specific runoff routing is the separation of drainage network into river stretches, lakes or reservoirs, and floodplains. Unfortunately, the reservoir database used in PCRGlobwb does not include the major reservoirs in either the Ca or the Downstream Red River basins.

This study uses the results of global simulation of PCRGlobwb done by the Department of Physical Geography of Utrecht University using the combination of ERA-40 and ERA-Interim daily climate data as the input [48]. Since PCRGlobwb only allows transpiration to extract water from the first and the second soil layers, the unsaturated zone storage is then calculated as the combination of storage in these soil layers. The unsaturated zone ΔS is the difference between storage in the first day of the next month and the first day on the current month. The unit of soil moisture in Store 1 and Store 2 is in meter; therefore a conversion to millimetre was done to get consistent results with the other estimation methods.

Unfortunately, the spatial resolution of PCRGlobwb's outcomes are only available at 10 km. Hence, a downscaling process was performed to the total monthly unsaturated zone storage using monthly NDVI datasets as proxies. The downscaling method used in this process is the same as the one performed in Method 1. More detailed explanation of the downscaling process is provided in Section 2.6: Downscaling Process.

2.3. Land-surface Model: GLDAS-Noah

Land surface models are developed to investigate the dynamics of land and atmosphere interactions to improve climate models and numerical weather predictions [23, 24]. In particular, they are meant to capture the variability of terrestrial energy and hydrological fluxes/stocks as a response to near-atmospheric forcing.

Unlike hydrological models, land surface models derive ET flux from the coupling of water and energy balance simulations. They are also able to use the Regional Climate Model (RCM) output more extensively. This particular trait has made land surface model as the more potential tool to accurately estimate water partitioning within the hydrological cycle [24]. However, the fact that land surface models have a more complex structure and a high number of parameters made the parameterization process rather difficult compared to most hydrological models. Traditionally, this process is done using a global land surface classification scheme based on various landscape or vegetation indices [23]. The leading examples of land surface models are those under the GLDAS scheme.

GLDAS is a global system that has been developed jointly by NASA-GSFC and NOAA-NCEP to address the problem of land surface model parameterization. They constrain the states and fluxes in the land surface model using data obtained from state-of-the-art ground and space observation systems. The constraints themselves are applied in two different ways; by using observation-based meteorological forcing to avoid biases that come from atmospheric model-based forcing and by employing data assimilation technique in order to make sure that the model does not produce unrealistic result [38]. Another benefit of the LSMs under GLDAS is the ability of those models to produce various continuous estimates of land surface states and fluxes in a high spatial resolution (i.e. 0.25^o and 1°) and timescale (i.e. 3 hourly, daily, and monthly).

A recent development was made by NASA by introducing a more consistent climatic forcing into the GLDAS land surface models. The forcing itself, produced by Princeton University, is a reanalysis meteorological product that has undergo a bias correction process using an observation-based dataset [7]. The product is called GLDAS-2 and it covers the period of 1948 to 2012.

Noah is 1 of the 4 LSMs that are currently run by GLDAS. It was first introduced in 1993 as a core project within the Global Energy and Water Cycle Experiment (GEWEX) Continental-Scale International Project (GCIP) that was spearheaded by NCEP. The original purpose of its development was to create a modern LSM for NCEP's weather and climate prediction models and the data assimilation systems which can be accessed freely by the hydro-meteorological community [14].

Noah is a 1-D column model that can be coupled or uncoupled to atmosphere. It incorporates the soil-vegetation-atmosphere transfer scheme (SVATS) into its model structure to simulate the states and fluxes. Hence, vegetation and soil properties are significant in the model parameterization process. Noah uses at least 37 parameters where 10 of them are related to vegetation properties, 11 are soil properties dependent, and the rest are universal parameters [33]. Soil is divided in to 4 different depths; 0-10 cm, 10-40 cm, 40-100 cm, and 100-200 cm. The outputs are frozen soil moisture, liquid soil moisture in 4 soil layers, soil temperature, skin temperature, snow pack depth, snow pack water equivalent, canopy water content, and the energy and water fluxes within the coupled water and energy balance. The concept behind Noah is presented in Figure 2.5.

The key flux in land-surface simulation in tropical regions is bare soil evaporation and plant transpiration. This flux hugely influences the variability of streamflow and change in the soil moisture storage. The nonlinearity in the direct evaporation process means that as water content in the top millimetres of the soil declines, the top soil becomes drier and acts as a barrier to dampen the rate of direct evaporation. This phenomenon is modelled using Eq. 2.8 and Eq. 2.9.

$$FX = \frac{\Theta_1 - \Theta_{dry}}{\Theta_{sat} - \Theta_{dry}} \tag{2.8}$$

$$E_{dir} = \left(1 - \sigma_f\right)(FX) f_x E_p \tag{2.9}$$

Where:
FX = fraction of the saturated soil
Θ_1 = top soil moisture
$\Theta_{dry}, \Theta_{sat}$ = dry and saturated soil moisture
f_x = empirical coefficient to indicate nonlinearity in the process of evaporation
$\left(1 - \sigma_f\right)$ = non-vegetated fraction in the grid cell
E_p = potential evaporation
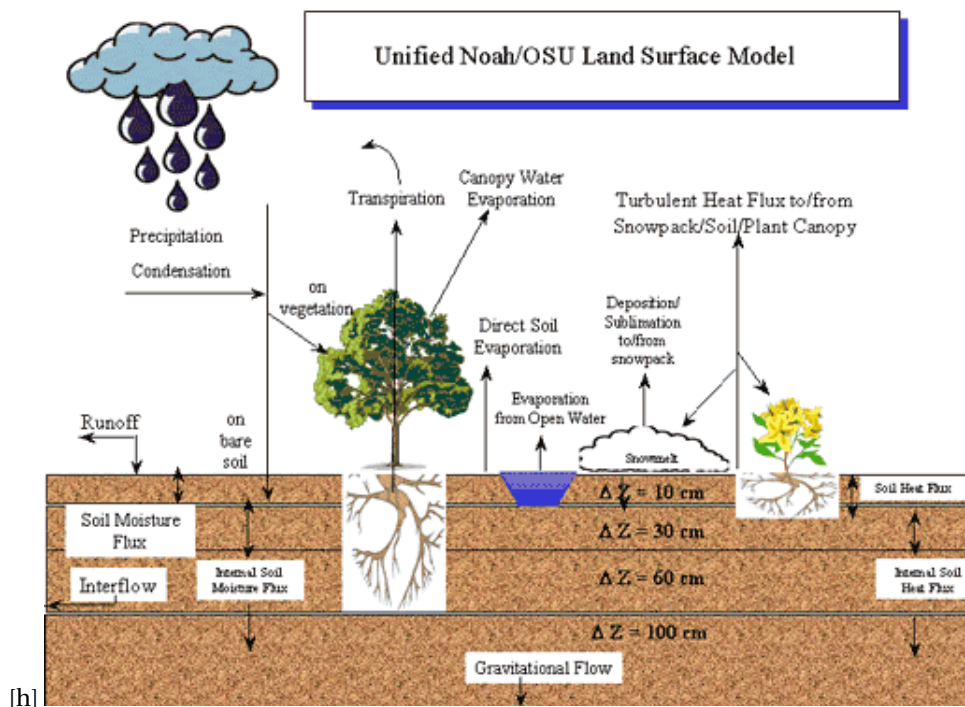
Figure 2.5: Simplification of the GLDAS-Noah model structure

The other significant component is plant's transpiration. Noah models the seasonality of vegetation using temporally and spatially varying green vegetation fraction (σ_f) based on NDVI information. Noah's default land cover parameter is derived from IGBP MODIS 20-category vegetation. Land-water mask is derived from the new MODIS land-water mask at 250 m (MOD44W) while elevation and soil texture data are obtained from GTOPO30 and the combination of STATSGO/FAO soil classification. However, little attention is put on the lateral movement of energy and water on ground surface and underground, such as the lateral subsurface flow between grids and grids along the slope [7]. This neglect may lead to the overestimation of water storage in soil layers.

The finest spatial resolution produced by Noah is 0.25$^{\text{o}}$ x 0.25$^{\text{o}}$, or almost equivalent to 25 km in the equator. The sub-grid variability is applied within the model using a mosaic approach. This is done through several steps. First, the land cover classes that are present in each Noah's grid are identified. The coverage area of each class within one grid is treated as a weight factor. The land cover mask is based on a 1 km global vegetation dataset. Second, Noah is run on a series of individual soil column where each column represents a single land cover class. Finally, the total average grid value is obtained by combining the weighted tiles' value [38]. The temporal resolution for the Noah product is 3-hourly. The monthly product is obtained by averaging the 3-hourly products.

This study used the monthly product of GLDAS-Noah version 2.0 with a spatial resolution of 0.25$^{\text{o}}$ [37]. Since the spatial resolution is very coarse, a downscaling process was implemented, using monthly NDVI dataset as proxy. The unsaturated zone is calculated as the combination of three Noah soil layers (i.e. 10-40 cm, 40-100 cm, and 100-200 cm). The unit of soil moisture content in each soil layer is kg/m^2. A conversion was done using the density of water to get the volumetric soil moisture content. The unsaturated zone ΔS is calculated by subtracting storage in the first day of the current month from the first day of the next month. The final ΔS products are calculated in millimetres.

2.4. Budyko Curve

Budyko Curve is a framework that explains the relationship between climatic condition and water balance in a certain basin. It is physically based on the combination of annual energy and water balance with an assumption that the basin is in a steady state condition [13]. The steady state water and energy balance are presented in Eq. 2.10 and Eq. 2.11.

$$\Delta S = P - ET_a - Q$$
$$P = ET_a + Q$$
(2.10)

Where $\Delta S = 0$ and water balance is at steady state.

$$\Delta E = R_n - \lambda \rho E - H - G$$
$$R_n = \lambda \rho E + H$$
(2.11)

Where the soil heat flux (G) is approximately 0 and energy balance is at steady state.

In the most practical sense, Budyko Curve can be used to partition mean annual precipitation into mean annual surface runoff and mean annual total evaporation and transpiration. The original Budyko Curve is shown in Figure 2.6.
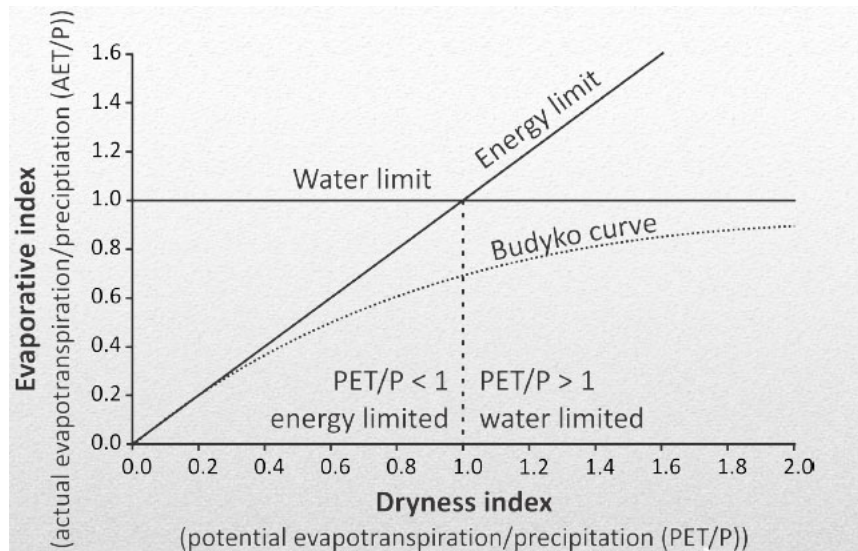
Figure 2.6: The Budyko Curve

The vertical axis of Budyko Curve is the ratio of actual ET over supply of water, or what is commonly known as the evaporative index (ϵ). If the evaporative index approaches unity, the area has sufficient energy to evaporate water from the surface and the soil layers. The rate of ET will only be limited by the amount of water supply in the area. On the other hand, the horizontal axis shows the ratio of potential ET over the water supply or the aridity index (Φ). Lower values of the aridity index refers to less available energy to evaporate water in the area, hence it is said that the area is energy constrained. In a steady state condition, the supply of water in a certain area is solely coming from precipitation. However, the steady state condition is rarely achieved since influence of terrestrial ΔS on the supply of water is rather significant, especially in irrigated agricultural fields or in between the drought periods [50].

Deviation from Budyko Curve in many different basins has been a topic of various researchers. Among other factors, the terrestrial ΔS and the influence of vegetation cover seasonality are the two most nominated causes [13, 32, 51, 53].

Following the same understanding as previous researches, this study tries to implement the Budyko Curve framework on to the partition of water in a monthly water balance. Even though Budyko Curve is meant for a long term and steady state water balance analysis, this study assumes that Budyko Curve is also applicable for monthly and unsteady water balance analysis.

The sequence of equations shown by Eq. 2.12 explains the hypotheses mentioned before.

$$\Delta S = P - ET_a - Q$$
$$\Delta S = (P - Q) - ET_a$$
$$\Delta S = ET_p - ET_a$$
(2.12)

The first line in Eq. 2.12 is an unsteady monthly water balance. The second line shows the rearrangement of elements of the first line. It shows that monthly terrestrial ΔS is the residual of the incoming flux and the

outgoing flux. To close the water balance, potential ET should makes up the difference between P and Q. Most of the times, actual ET differs from potential ET. Therefore monthly terrestrial ΔS can be explained as the difference between monthly potential ET and actual ET. Moreover, although ΔS in above equations refer to the bulk term of terrestrial ΔS, this study assume that the influence of unsaturated zone ΔS variability is more significant than the surface or the groundwater component.

The reference potential ET is described as a combination of water that is going to be extracted from soil surface and water that is generated by plants' biophysical activities if the process is not limited by actual supply of soil moisture. In other words, reference ET is the physical representation of atmospheric demands of evaporated and transpired water. It is solely influenced by climatic condition. FAO describes reference ET as the amount of water that is evaporated and transpired from a hypothetical grass covered surface with specific characteristics [4]. The most common method to quantify reference ET is the Penman-Monteith formula as shown in Eq. 2.13 below.

$$ET_p = \frac{0.408\Delta\left(R_n - G\right) + \gamma\dfrac{900}{T+273}u_2\left(e_s - e_a\right)}{\Delta + \gamma\left(1 + 0.34u_2\right)} \tag{2.13}$$

Where: ET_p = reference ET (mm/day)
R_n = net radiation at the crop surface (MJ/(m^2.day))
G = soil heat flux density (MJ/(m^2.day))
T = mean daily air temperature at 2 m height (^{o}C)
u_2 = wind speed at 2 m height (m/s)
e_s = saturation vapour pressure (kPa)
e_a = actual vapour pressure (kPa)
$e_s - e_a$ = saturation vapour pressure deficit (kPa)
D = slope vapour pressure curve (kPa/^{o}C)
g = psychrometric constant (kPa/^{o}C)

This study uses the monthly reference ET values which were calculated using a mathematical model based on the Penman-Monteith formula. The input needed to force this model and their sources are shown in the Table A.3 in the Appendix section.

On the other hand, actual ET is equal to the amount of water that is actually being evaporated and transpired from the soil surface. The present soil moisture is the limiting factor. The amount of the present soil moisture is influenced by many physical factors aside from the climatic demand such as antecedent soil moisture condition, soil type, land cover and land use type, the amount of occurring precipitation, etc. This study uses an ensemble ET product to represent actual values of ET in both the Ca and the Downstream Red River Basin [36, 42].

The precipitation dataset for the Downstream Red River Basin uses the TRMM 3B43 product from NASA [29] while the Ca River Basin uses an ensemble precipitation product derived from TRMM 3B43 from NASA [29] and CHIRPS from the Climate Hazard Group [19].

The unit of the monthly actual and potential ET and the monthly precipitation input is millimetre. The final monthly ΔS products are also in millimetre.

2.5. Validation Process

This study adopts 2 validation approaches to determine which method is the optimum for WA+ application. The first approach is the evaluation of each method's ability to regenerate the sub-basin average observed river discharge at the streamflow measuring stations and the streamflow-derived ΔS. In addition to that, since comparison using spatially average values can lead to inter-pixel compensation and also considering the high spatial variability of ΔS, the relationship between land use and land cover classes and ΔS values needs to be evaluated as well. More detailed explanation on each approach is provided in the following subsection.

2.5.1. Comparison to the observed streamflow and the streamflow-derived unsaturated zone ΔS

The first comparison is to the streamflow observation in different measuring stations. First, the estimated monthly streamflow from each method is computed using pixel-based water balance equation with climate

input (i.e. P and actual ET from remote sensing products) provided from Poortinga et al. [36] and Simons et al. [42] and the estimated ΔS. The pixel-based monthly water balance is shown in Eq. 2.14.

$$Q_{est,monthly} = P_{RS,monthly} - ET_{RS,monthly} - \Delta S_{est,monthly} \tag{2.14}$$

The next step is to perform sub-basin delineation in the Ca River Basin and the Downstream Red River Basin to match the correct drainage area to the location of streamflow stations. The location of the streamflow stations in both the Ca and the Downstream Red River Basin is shown in Figure 2.7.
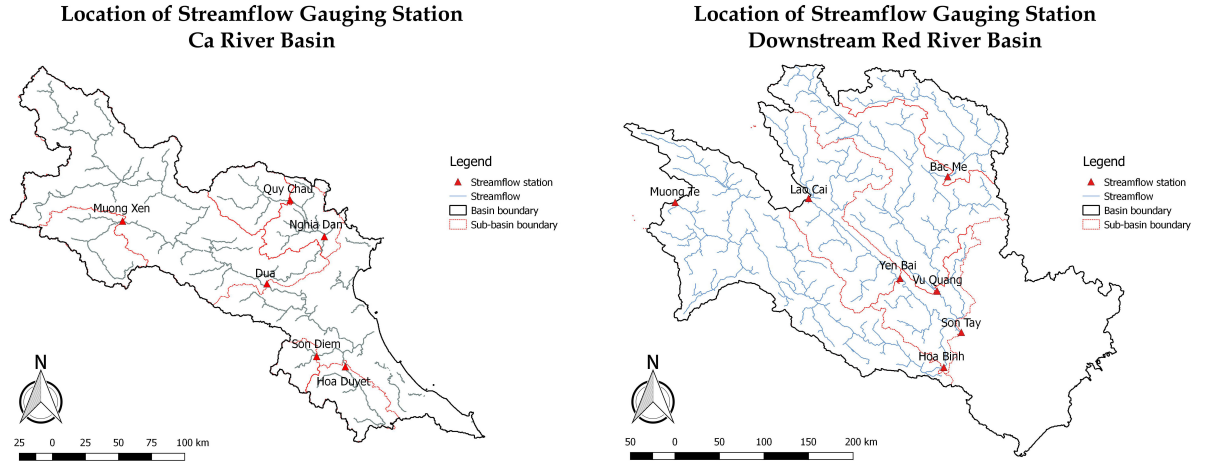
Figure 2.7: The locations of the streamflow stations and their drainage areas in the Ca and the Downstream Red River Basin

After the sub-basins are identified, both the observed and estimated streamflow are averaged spatially over the area of the sub-basins. Finally, the estimated streamflow values are compared to the observed streamflow values in each station.

The steps for the unsaturated zone ΔS comparison are similar to what is written above. The only difference is that instead of directly measured values, a derivation from streamflow observation is used as the reference for the validation. This is calculated using a point-based monthly water balance equation similar to Eq. 2.14. The equation is shown in Eq. 2.15 below. The P and the actual ET inputs are the same as the one used in Eq. 2.14.

$$\Delta S_{obs,monthly} = P_{RS,monthly} - ET_{RS,monthly} - Q_{obs,monthly} \tag{2.15}$$

The performance of each estimation method is then evaluated using weighted R^2 and RMSE. These mathematical measures evaluate different aspects of the fit between the observed and estimated values. The Root Mean Square Error or RMSE is the square root of variance of the residuals. This parameter is often seen as the absolute measure of the fit between observed and estimated values. Lower values of RMSE indicate better performance of the model in regenerating observed values. The R^2 tells how good the dispersion of the observed values explains the dispersion of the estimated values. Lower R^2 values are equal to small correlation between the observed and the estimated values; whereas R^2 values of 1 show that the estimated values are equal to the observed ones. However, R^2 should not be used alone since it only accounts for the dispersion. This study uses weighted R^2 which is a combination of slope of the correlation and R^2. A good method should generate a near-1 weighted R^2 value [28]. The Eq. 2.16 below explain the rules for the weighted R^2. b represents the slope of the relationship between the estimated and the measured values.

$$wR^2 = \begin{cases} |b| \cdot R^2 \text{ for } b \leq 1 \\ |b|^{-1} \cdot R^2 \text{ for } b > 1 \end{cases} \tag{2.16}$$

2.5.2. Spatial distribution correctness
The second approach is meant to check the ability of each estimation method to recreate the spatial distribution of land use and land cover classes. It is important to note that this approach is based on the hypothesis

that there is a correlation between the types of land and/or vegetation cover to the magnitude of the unsaturated zone ΔS.

The first step is to calculate the average unsaturated zone ΔS value in different land use land cover classes for each method. Next, these values are plotted in time. The purpose is to check whether there are any out-of-place behavioural trends that can be observed (e.g.: the irrigated crop fields generate more water than the forest land cover type, etc.). Second check for the spatial distribution correctness is done by plotting the entire unsaturated zone ΔS pixels generated from each estimation method and grouped them based on their corresponding land use and land cover class.

2.6. Downscaling Process

The goal of this study is to produce a spatially distributed estimation of the unsaturated zone storage change with a fine spatial resolution. The spatial quality of the product is heavily dependent on the input datasets. Unfortunately, most of the input datasets used in this study are only available in lower spatial resolutions, with 50 km being the coarsest spatial resolution to be dealt with. On the other hand, information such as the NDVI dataset is available at a very fine spatial resolution (i.e. 250 m). While it is understood that the quality of the outcome will only be as reliable as the coarsest input dataset, using medium to low spatial resolution will risk the study to lose too much spatial information given by the fine scale input datasets. The example of the coarse input dataset and a fine proxy layer is shown in Figure 2.8. Starting from upper left going clockwise, the Wang-Erlandsson maximum root zone storage capacity with a pixel size of 50 km, the PCRGlobwb monthly unsaturated zone moisture storage with a pixel size of 10 km, the GLDAS-Noah monthly unsaturated zone moisture storage with a pixel size of 25 km, and the eMODIS NDVI with a pixel size of 250 m.
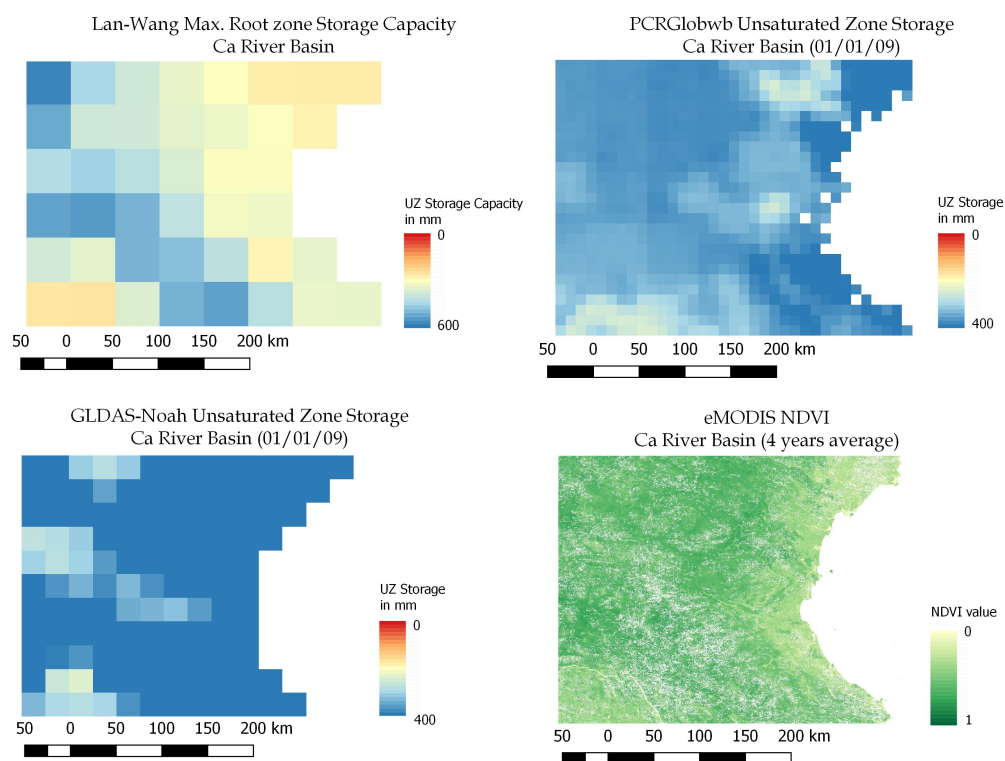
Figure 2.8: The example of the coarse resolution input dataset and a fine resolution proxy dataset of Ca River Basin

This study adopted the downscaling method developed by Agam et al. [3] for thermal imagery sharpening using NDVI, which then improved by Immerzeel et al. [25] using a coarse scale TRMM precipitation dataset and a set of finer scale NDVI datasets. Both of the downscaling methods mentioned above are based on the hypotheses that there is a unique relationship between the finer scale proxy layer (i.e. the NDVI dataset) and the coarse scale input layer (i.e. the Landsat temperature dataset and the TRMM precipitation dataset). This unique relationship is then used to project the spatial variability of the input variable from a coarse spatial

scale to a finer spatial scale. It is also important to consider that the spatial scale of the biophysical process to be disaggregated has to be larger than or, at the very least, equal to the spatial scale of proxy layer. Both of these conditions limit the options of finer resolution datasets suitable to become the proxy layer.

The steps taken in the downscaling process is explained through the flowchart shown in Figure 2.9. The regression applied in the thermal imagery sharpening by Agam et al. [3] was a second order polynomial regression while Immerzeel et al. [25] chose to use an exponential regression to define the unique relationship between TRMM and NDVI products. As mentioned in steps above, this study chose to follow Agam's footstep and used a polynomial regression to explain the relationship between the input and the proxy layer. However, it is also important to note that the quality of a polynomial regression is sensitive to the presence of either high or low outliers in the relationship between the input and the proxy data points. One way to overcome this is to apply a selection criterion before computing the parameters of polynomial regression such as screening out coarse pixels in the input dataset that correlate to high sub-pixel variability in the proxy dataset.
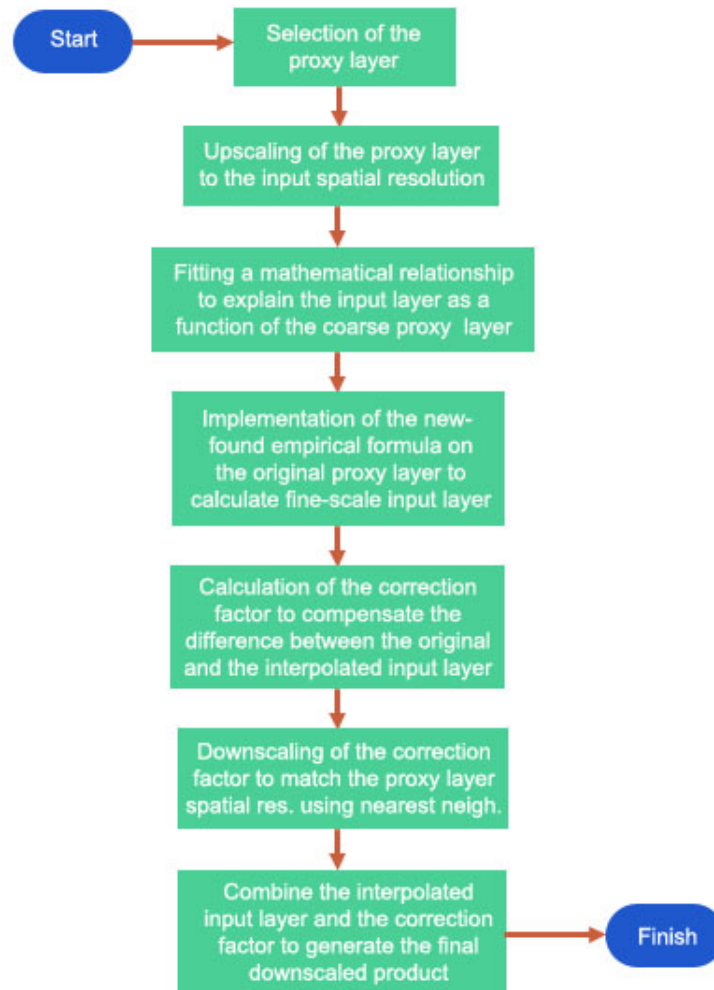
Figure 2.9: The downscaling process

3

Study Area

Like the rest of the Southeast Asian countries, climate in Vietnam is governed by the South Asian and Northeast Asian monsoon, the Pacific Tropical Cyclones, and the El-Nino Southern Oscillation (ENSO) events. Located in the humid sub-tropic, the northern part of the country experiences a more distinct summer and winter rainfall events while the tropical southern regions have a slightly more uniform rainfall pattern [30]. The start of the summer season varies from early May in the southern Vietnam to late July-August as it moves northward. The rainfall events in this season are dominated by the South Asian monsoon. The Northeast Asian monsoon mainly influences the rainfall events during winter months in the north and central regions. The long coastline of Vietnam is mostly vulnerable to the Tropical Cyclones rainfall events especially during June to November. In addition to the monsoonal system, the inter-annual climate variations in Vietnam are also driven by the ENSO which enhances the dry and warm conditions during El-Nino years. Given this high inter-annual variability, some regions can suffer from both flooding in the rainy season and drought during the dry season [17].

3.1. The Ca River Basin

The Ca River Basin is a trans-boundary river basin shared between Vietnam (65%) and the LAO People Democratic Republic or LAO DPR (35%). The total area of the Ca Basin is around 27,277 km^2. The Vietnamese Ca Basin occupies around 17,730 km^2 area in the north-central region of the country [1]. It is estimated to be inhibited by 4 million people from 8 different ethnic groups. Rainfall events are concentrated in the period between May and October, in accordance with the influence of the South Asian monsoon. In general, the peak rainfall occurs in September. However, the southern part of the basin usually experience heavier rainfall events compared to the northern regions [1]. The spatial distribution of monthly precipitation and actual ET on January and July is shown in Figure 3.1. The clear distinction between January and July indicates strong seasonality in the Ca River Basin. On average, January is drier compared to July where the amount of precipitation and actual ET is significantly lower than what was recorded for July. These two months are seen as the peak of dry and rainy season, respectively.

In total, the Ca River stretches for a distance of 531 km with 361 km of it runs over the Vietnamese landscape. The Ca River originates in Muong Khut and Muong Lap Mountain in LAO DPR. The main branch of the Ca River enters the Vietnamese border through Nge Anh Province, flows to the south-eastern direction before flowing out into the Eastern Sea via the Cua Hoi river mouth [18]. There are several tributaries feeding the main Ca River. The largest tributary is called the Hieu River which enters Vietnam through Thanh Hoa Province and flows southward to Nge Anh Province, joining the Ca River at the midstream. The second biggest tributary is the La River. It originates from the Giai mountainous area in Ha Tihn Province and joins the Ca River at Cho Trang confluence [1]. The discharge in the main Ca River before the confluence is measured by Dua Station. The observed monthly streamflow in Dua Station for the period of 2007 to 2010 is shown in Figure 3.2.

---

[1]Some documents consider an additional area of 2,650 km^2 into the Vietnamese Ca River Basin to account for the wetlands, lagoons, and smaller streams that bypass the main Ca River and flow directly to the Eastern Sea. This made the total area of Vietnamese Ca River Basin closer to 70% of the total Ca River Basin or around 20,460 km^2.

**Average January and July Precipitation and Actual ET
Ca River Basin**

(a) average precipitation on January

(b) average precipitation on July

(c) average ETa on January

(d) average ETa on July
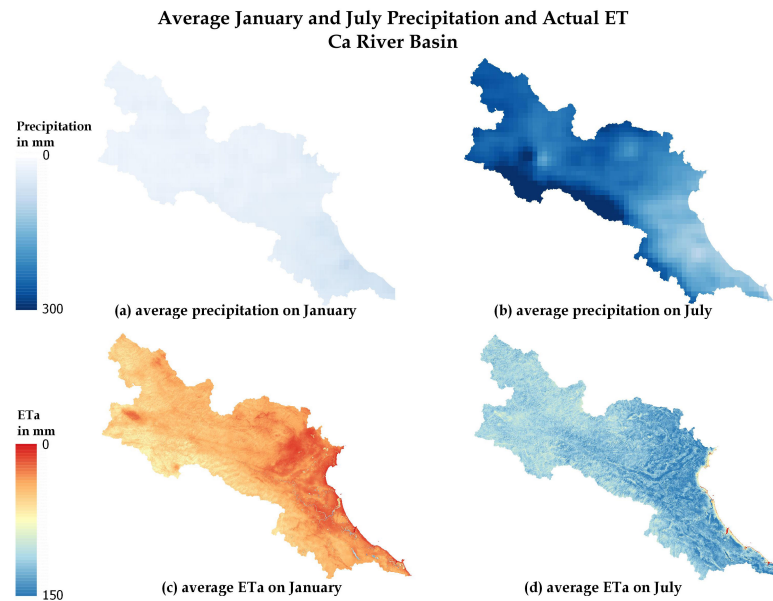
Figure 3.1: Average January and July precipitation and actual ET in the Ca River Basin
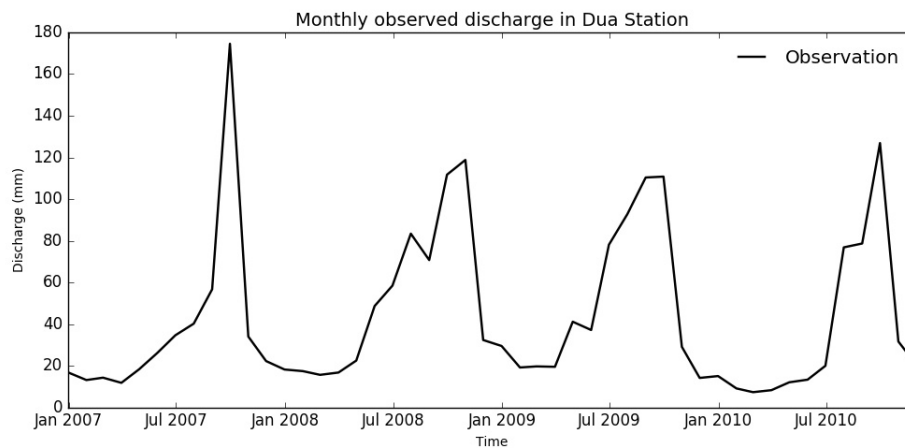
Figure 3.2: Monthly observed discharge in Dua Station

Although Nge Anh and Ha Tihn Province occupy the majority of the Vietnamese Ca River Basin, not all of the areas in the provinces are hydrologically connected to the Ca River. These disconnected areas receive water through a series of irrigation systems. Currently there are 3 large, operating, irrigation systems which not only provide water supply to the agriculture sector but also utilized to meet the domestic and industrial demands [36]. There are 5 major reservoirs included in the water supply system as shown in the information provided in Table 3.1 [2].

The unsaturated zone soil in the downstream of the basin is dominated by the Gleysols, the typical soil of lagoons, wetlands, and other areas with shallow groundwater table. Infiltration is low due to the fine texture of the soil particles and frequent water logging conditions. In the mountainous area in the upstream of the basin, the soil is mainly comprised of the Acrisols, a soil type typical to the wetter part of tropical countries.

The land use and land cover map used in this study is the one developed by Poortinga et al. [36] for his study about the partitioning of water in the Ca River System. As shown in Figure 3.3, the three major land-use classes are the secondary forest, the irrigated rice fields, and the broadleaved forests. The upstream part of the basin is dominated by the secondary forest class followed by a smaller portion of rain fed rice fields. The secondary forest functions as the producer of goods and services for the local livelihood. The intensive

---

[2]A = Agriculture, I = Industry, M = Maintenance of normal flow, P = Hydro power, F = Flood control, W = Municipal water supply

River Name	Dam Name	Catchment Area (km^2)	Gross Capacity (10^6 m^3)	Effective Capacity (10^6 m^3)	Purpose	Year of Completion
Ca	Ban Ve	8,700	1,834.6	1,383	A, I, M, P, F	2009
Hieu	Ban Mong	2,785	252.6	125.8	A, I, M, P	2012
Ca	Khe Bo	14,300	97,8	17.2	P	2010
Giang	Thac Muoi	785	558.1	437.8	P, F	-
Ngan Sau	Ngan Truoi	506	425.6	353.9	A, P, I, F, W	2014

Table 3.1: The list of major reservoir in the Ca River Basin

The Land Use and Land Cover in The Ca River Basin
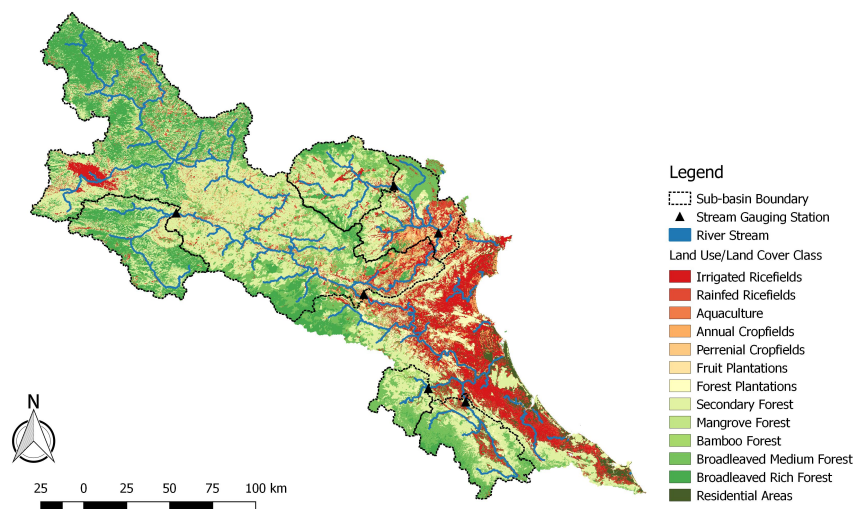
Figure 3.3: Land use and land cover information in the Ca River Basin

irrigated rice cultivation occupies most of the delta areas. There can be up to 3 harvests over a year, one for each season, with the summer rice cultivation (i.e. during May to August) being the staple farming practice. There are more farmers in Nge Ahn Province (45%) who practice 3 harvests per year compared to the farmers in Ha Thinh Province [36, 44].

3.2. The Downstream Red River Basin

The Red River Basin is a trans-boundary river basin which upstream is located in China and the rest of the basin is mainly located in Vietnam, with only less than 1% in LAO DPR. The main stream is around 1200 km long, originating in Yunnan Mountain in China and flows in the southeast direction to Vietnam before it drained into Halong Bay in the Eastern Sea. The part of the Red River Basin in Vietnam is regarded as the Downstream Red River Basin. It covers an extremely large area of 87,236.75 km^2 which comprised of 26 provinces in northern Vietnam, including Hanoi, the capital of Vietnam. The total population in the Downstream Red River Basin is around 28 million people with the majority of the population inhibit the Red River Delta area [10]. This basin is the second largest basin in the country after the Mekong River Basin in southern Vietnam. Consequently it also serves as the country second largest agricultural area, providing livelihood for around a third of the country population.

The Downstream Red River Basin is divided in to 5 sub-basins as shown in Figure 3.4 below. The names of the sub-basins and their main streams are the Da River, the Thao River, the Lo Gam River, the Upper Thai Binh River, and the Lower Red River. The Lo Gam and the Da River Basin are the two largest sub-basins [44]. The 3 mainstreams of the Downstream Red River Basin; the Da River, the Thao River, and the Lo River, join

in Viet Tri, upstream of Hanoi, to form the Lower Red River [1]. The Da River contributes the most discharge compared to the other main streams, making it as the most important source of water for the irrigation system in the Lower Red River Basin [8].The main streams of the Red River also carry huge quantities of silt originating from the upstream area in China. This alluvium silt contributes greatly to the development of the agriculture activities in the Red River Delta [47].

The Land Use and Land Cover in The Downstream Red River Basin
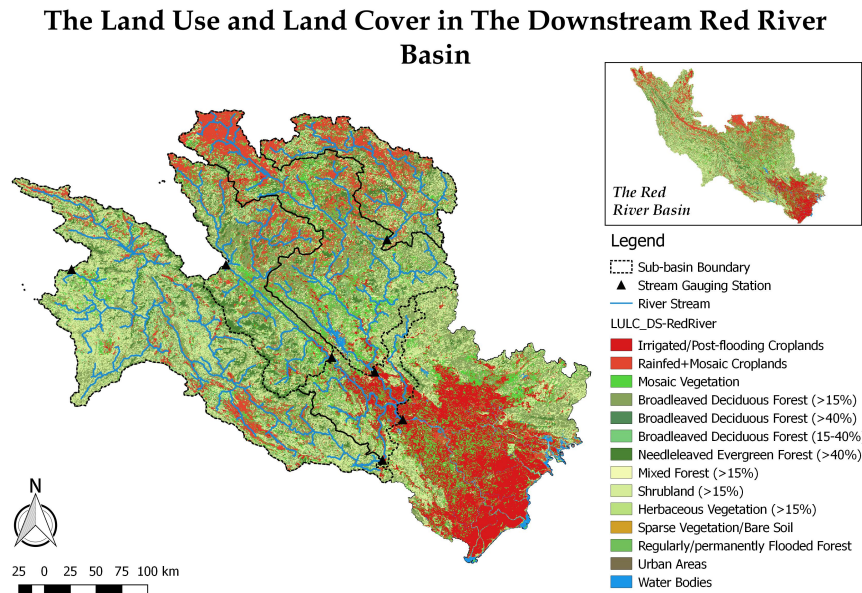
Figure 3.4: Land use and land cover information in the Downstream Red River Basin

The typical wet months in the Downstream Red River Basin occurs during the summer season, from May to October. The wet season is characterized by a high net radiation value, a high temperature, and moderate relative humidity. This season is followed by the dry season with low net radiation, low temperature, and low relative humidity. The dry season usually lasts from October to January. The months between the dry and the wet season (i.e. February to April) is known as the intermediate season, which is characterized with moderate to low temperatures and a high relative humidity. From a long-term time series analysis, it is found that the annual rainfall over the basin's vast area varies extremely between 700 to 3000 mm [42]. The spatial distribution of the monthly precipitation and actual ET on January and July is shown in Figure 3.5. Similar to what was found in the Ca River Basin, precipitation and actual ET on January is significantly lower than what was found for July.

The high rainfall variability between wet and dry season leads to the variability and irregularity in the river discharge, with June to October regarded as the peak flow period [8]. The flow through the basin is unequally distributed in space and time which leads to two extremes condition; drought during the dry winter season and flooding in the wet summer season. The low flow during the dry period also causes the rise of salinity in the river since it draws back saline water from the Eastern Sea to the river system [42]. The dynamic of the streamflow in the Downstream Red River Basin is shown in Figure 3.6 below using measurement in Son Tay Station, the most downstream station in the basin.

This study adopted the land use and land cover map developed by Simons et al. [42]. The highlands area in the basin is characterized by hilly and mountainous terrains whereas the lower part of the basin is mainly formed by wetlands. The highlands are mainly comprised of a mixture of forest classes with a small fraction of agriculture lands where dry crops (e.g. rain fed rice, vegetables, or maize) are grown. The lower Downstream Red River Basin is also known as the Red River Delta. The area is a rich-agriculture growing area, where an intensive rice cropping activity is practiced by most of the farmers. Currently there are 4 major reservoirs being operated in the Downstream Red River Basin to provide service for the agriculture fields and the hydropower plants. The biggest reservoir is the Hoa Binh reservoir which located in the Da River Basin [10].

As the principal crop, rice is harvested all year round. However, without irrigation systems, rice can only

**Average January and July Precipitation and Actual ET
Downstream Red River Basin**

(a) average precipitation on January

(b) average precipitation on July

(c) average ETa on January

(d) average ETa on July
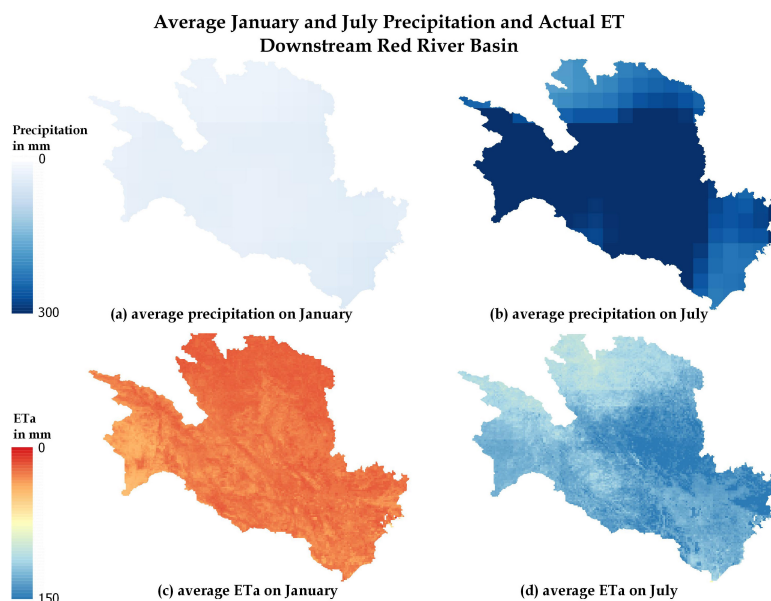
Figure 3.5: Average January and July precipitation and actual ET in the Downstream Red River Basin
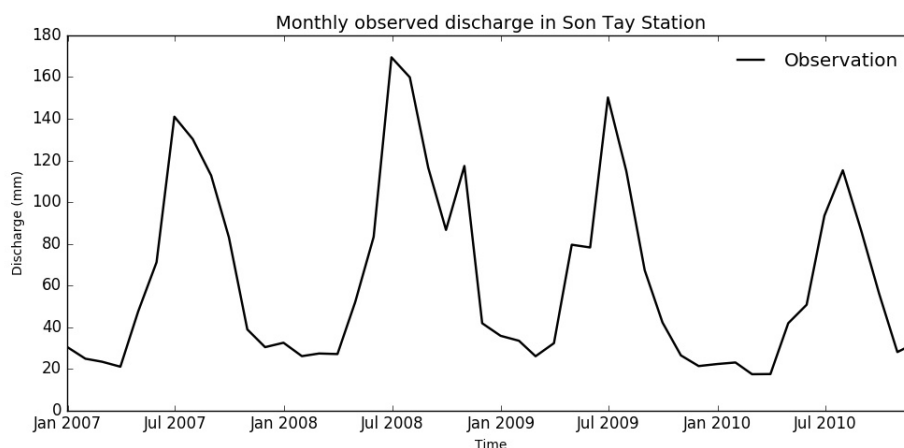
Figure 3.6: Monthly observed discharge in Son Tay Station

be grown once per year during the wet summer season. A second rice cropping period usually occurs during the spring season with the help of irrigation. Hence, the irrigation systems are an integral part of the Red River Delta. A study in 2012 noted that there are 31 irrigation schemes in the Red River Delta, providing water supply for approximately 8,500 km^2 irrigated rice fields [8]. The irrigation water is also being recycled within the irrigation schemes. This has becomes a substantial source of water for the more downstream farmers [42].

The other type of dominant land use class in the Red River Delta is the urban areas with Hanoi as the most overpopulated and overdeveloped region in the class. Often hit by the recurring summer floods, the main protection infrastructure in the city and its surrounding areas is a system of two series of dykes with a total length of 2,700 km [8]. Aside from the flood events, the Red River Delta also experiences a serious water quality issue as the pollution from the industries and domestic use in the upstream areas increases over the last decade [10].

4

Result

4.1. Unsaturated Zone ΔS Estimation Methods

The estimated unsaturated zone ΔS in both the Ca and the Downstream Red River Basin is shown in Figure 4.1 and Figure 4.2. To highlight the importance of seasonal trend, only the results for January and July are included in the figures. The peak of the rainy season and, consequently, the primary rice farming season occurs on July each year. On the other hand, January is when the dry season in its peak and when the farming activities rely mainly on the irrigation system.

4.1.1. Ca River Basin

Two important aspects in the spatial distribution of the unsaturated zone ΔS in the Ca River Basin can be observed from Figure 4.1; the seasonal and the land use/land cover spatial distribution trend. Methods that are able to generate consistent temporal trends are the downscaled PCRGlobwb and the STREAM model. The results from these two methods consistently show distinctive dry and rainy months over the 4 years period (2007 to 2010), where July is generally wetter than January. Both also generate a more negative unsaturated zone ΔS in the upstream area during the dry month (i.e. January) which can be caused by the extraction of water due to farming activities in the secondary forest class. However, there is a difference in July where the downscaled PCRGlobwb products show more positive unsaturated zone ΔS in the forest class compared to the cultivated land class, while the STREAM model results show the opposite trend.

Seasonal trend can also be observed from the downscaled GLDAS-Noah results however it is less obvious than the PCRGlobwb and the STREAM model. July is mostly wetter than January, with the exception of 2008. Despite the obvious remnants from the coarse pixel size of the original GLDAS-Noah product, a finer land use/land cover based-spatial distribution trend can still be observed for January in 2007, 2008, and 2010, and July 2007 and 2009. The next method to show a seasonal trend is the Budyko Curve, where January is generally drier than July. A distinctive characteristic is observed from the July results where the northeast part of the basin is consistently drier than the rest of the basin. According to the land use and land class map, this part is a mixture of broadleaved forest, secondary forest, and rain fed crop fields. On July 2008 and 2010, the cultivated part of the basin extracts more water than the natural landscape. During the peak dry season, 2007 and 2008 are the wetter years compared to the 2009 and 2010.

The last two methods, the empirical relationship of Method 1 and WaterPix show similar results in terms of seasonal trend inconsistencies. The results from WaterPix show that January is generally a wetter period compared to July in 2007 and 2010. During 2007, the cultivated land class in the downstream part of the basin experienced a more negative unsaturated zone ΔS compared to the natural landscape in the upstream. The opposite happened in 2010 where the forested upstream extracts more water than the cultivated downstream. In 2008 and 2009, July is wetter than January. Both also show a more negative unsaturated zone ΔS in the forested upstream compared to the cultivated land class. A very clear change in unsaturated zone ΔS values can be seen in the upstream part of the basin. This follows the slicing process that had to be performed when running the model.

The seasonal trend in Method 1 switched after 2 years, where initially January is the drier month and July is the wetter month. The general spatial trend of this method is that the cultivated downstream area extracts less water compared to the natural landscape in the upstream area. The only exception is January 2008 where

the irrigated crop field land cover class shows a more negative unsaturated zone ΔS. Spatial distribution of the unsaturated zone ΔS of this method closely follows the spatial distribution of the downscaled Wang-Erlandsson et al. [52] maximum rooting depth.

Overall, the STREAM model results show the narrowest range of unsaturated zone ΔS values followed by the downscaled PCRGlobwb, Budyko Curve, downscaled GLDAS-Noah, WaterPix, and the empirical relationship of Method 1.
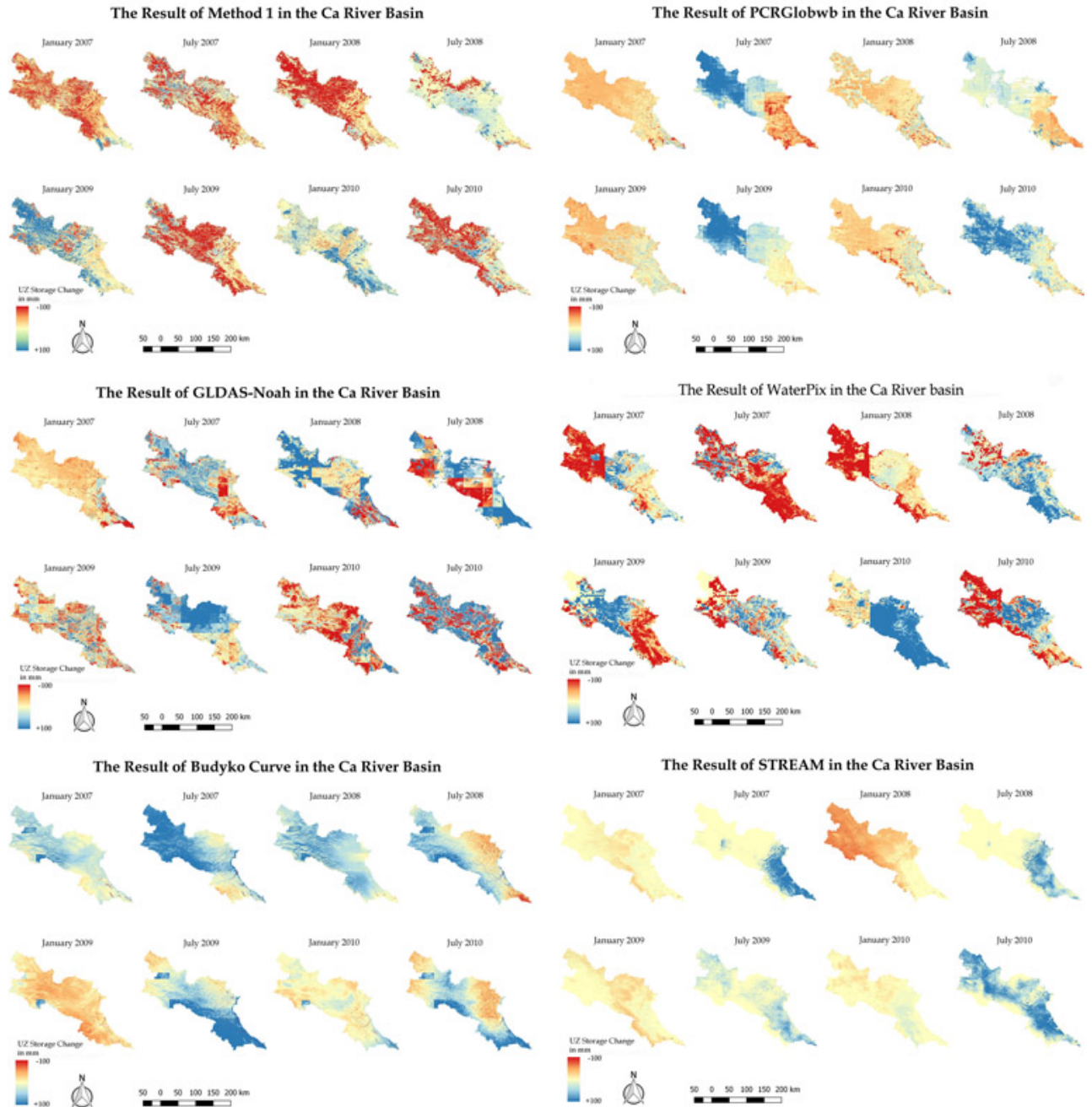
Figure 4.1: The estimated unsaturated ΔS results in the Ca River Basin

4.1.2. Downstream Red River Basin

The result of each estimation method in the Downstream Red River Basin is shown in Figure 4.2. Similar to the Ca River Basin, the seasonal-based variation and the land use/land cover spatial distribution are the two

aspects to be evaluated. Generally, the seasonal trend in the Downstream Red River Basin is more obvious than in the Ca River Basin. The difference between the peak of wet and dry season is clearer, where July is the wetter month and January is the drier month. Four out of the five methods applied in this basin show that 2008 is the driest year over the course of the observation period and that during January 2010 the central part of the basin generates more water than the rest of the area. The exception is generated by the Budyko Curve method.
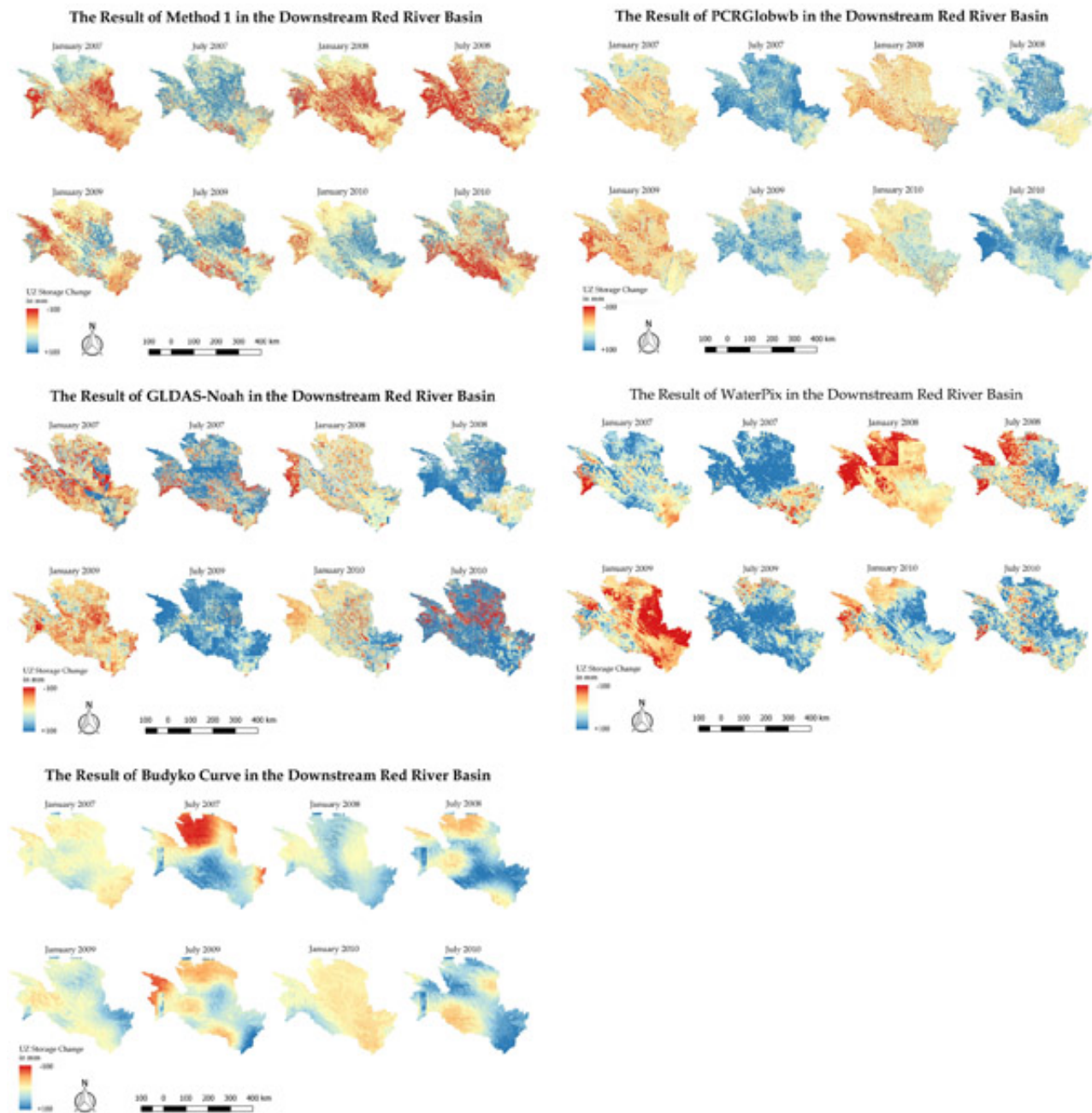
Figure 4.2: The estimated unsaturated ΔS results in the Downstream Red River Basin

Both the downscaled PCRGlobwb and the downscaled GLDAS-Noah generate similar results in terms of consistency in seasonal variation. However, the spatial distribution of the downscaled PCRGlobwb products agrees more with the spatial distribution of the land use/land cover classes. The results from this method show a more positive unsaturated zone ΔS in the upstream part of the basin which correspond to the location of the forested area. The more negative unsaturated zone ΔS is generated in the lower part of the

basin, where the intensive irrigation schemes are located. The result of July 2009 is even able to show a more negative unsaturated zone ΔS in the small patches of rain fed crop fields in the northern part of the basin. Meanwhile, the spatial distribution of the downscaled GLDAS-Noah products does not seem to reflect the spatial distribution of the land use and land cover classes. The results in January 2007 and 2009 show more wet pixels where the intensive irrigation schemes are located. Due to the size of the basin, the remnants of the coarse original GLDAS-Noah pixels size seem less obvious compared to the Ca River Basin.

The results from WaterPix also show a consistent seasonal variation where January is generally drier than July. The results show that the intensive irrigated land cover class extracts more water than the rest of the basin, with an exception of January 2008 and 2009. The empirical relationship of Method 1 also generates similar result to the downscaled PCRGlobwb, the downscaled GLDAS-Noah, and WaterPix except for June 2010. Two distinctive features that can be observed from this method are the similar range of unsaturated zone ΔS values for the intensive irrigated land class regardless the season and the consistent appearance of dry pixels in the western part of the basin every July.

The results of the Budyko Curve method have less agreement with the other methods in term of seasonal variation. However there is a distinctive feature that can be observed in each season. Firstly, dry pixels consistently appear in the northwest, northeast, and southwest of the basin every July. These area correspond to the mixture of rain fed and irrigated crop field and the natural landscape classes. The unsaturated zone ΔS in those areas is even more negative than what was found in the intensive irrigation pixels. Secondly, the spatial distribution of the unsaturated zone ΔS during the peak dry season (i.e. January) is more homogenous compared to the wet summer season.

4.2. Validation to the Observed Values

4.2.1. Ca River Basin

Both the estimated unsaturated zone ΔS values and the estimated discharge in the Ca River Basin from each method were compared to the observed values in 6 different streamflow stations. Figure 4.3 shows the comparison of the unsaturated zone ΔS and the discharge in Dua Station. Dua station is the station with the largest drainage area in the Ca River Basin, accounted for almost 76% of the total Ca River Basin area. For the sake of simplicity, the streamflow-derived unsaturated zone ΔS is going to be called as the observed unsaturated zone ΔS.
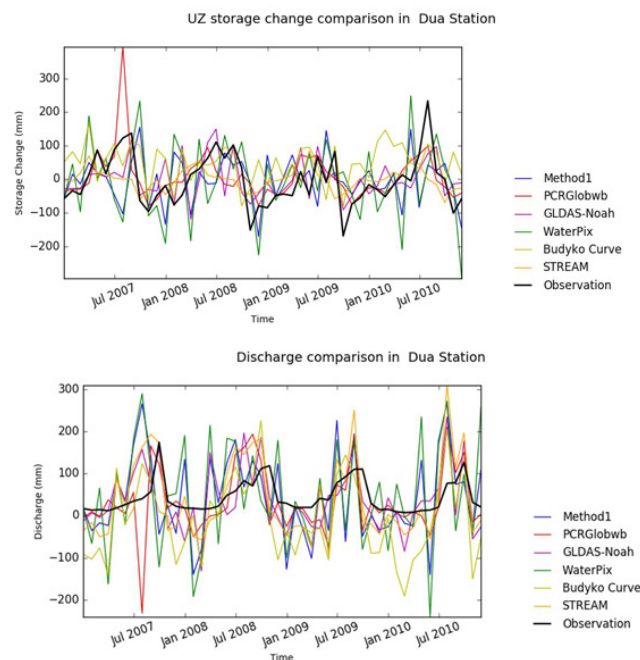
Figure 4.3: The unsaturated zone ΔS and the discharge comparison in Dua Station

From the figures above, it can be seen that the results from Method 1 and WaterPix show similar dynamic where the peaks and lows are generated in similar timing and magnitude. With the exception of the year 2007, the results from the downscaled PCRGlobwb, the downscaled GLDAS-Noah, and the STREAM model are all quite similar to each others. Out of the 6 different methods, the Budyko Curve results have less similarity towards other methods. However, apart from the similarities of one method to the others, none of them are able to replicate the observed peaks and lows in Dua Station correctly, both temporally and in magnitude.

Figure 4.4 shows the comparison of each method to the observed ΔS values. The distribution of the colourful markers around the 1:1 black line shows how well the estimated method approaches the real condition in Dua Station. From this figure, it can be seen that the downscaled PCRGlobwb has the least dispersion of markers around the black line while WaterPix has the most dispersion. The Budyko Curve seems to overestimate the ΔS values while the estimated ΔS from the STREAM model are often close to 0 mm.
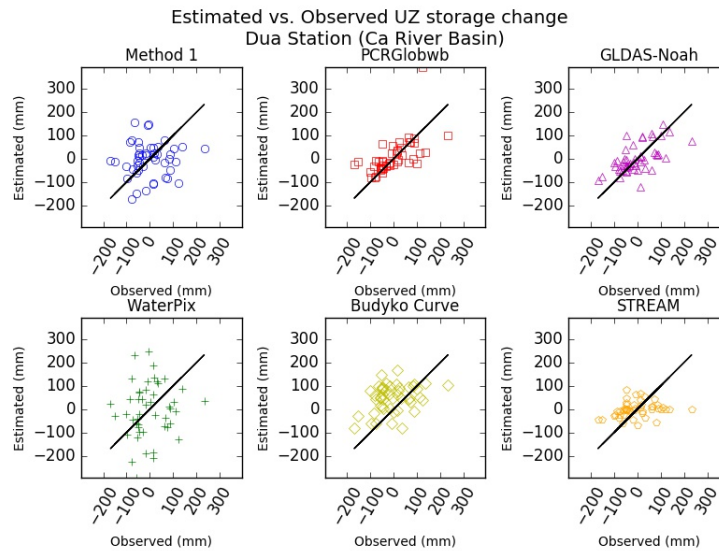
Figure 4.4: The comparison of each method to the observed unsaturated zone ΔS in Dua Station

Since the majority of water generated in the Ca River Basin drains to Dua Station, the statistical performance of this particular station is deemed representative for the whole Ca River Basin. The final basin-average statistical performance of each method is shown in Figure 4.5 below.
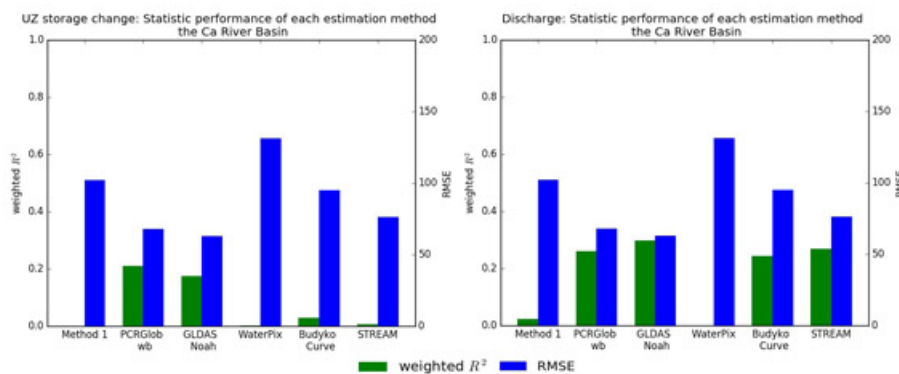
Figure 4.5: The comparison of basin-average statistical performance of each method in the Ca River Basin

Generally, the statistical performance of each method during the validation using the observed unsaturated zone ΔS is very poor while the discharge validation has better values. The STREAM model has better performance in replicating the observed discharge in the Ca River Basin (i.e. weighted R^2 = 0.27 and RMSE = 76.31), however it does not perform well in the estimation of the unsaturated zone ΔS (i.e. weighted R^2 =

0.006 and RMSE = 76.31). On the other hand, the downscaled PCRGlobwb has the highest performance in the unsaturated zone ΔS validation with weighted R^2 = 0.210 and RMSE = 67.84, and a moderate performance during the discharge validation with weighted R^2 = 0.26 and RMSE = 67.84.

4.2.2. Downstream Red River Basin

There are 7 streamflow measuring stations in the Downstream Red River Basin where 2 of them record the inflow from the upper part of the Red River Basin. The same as before, the estimated unsaturated zone ΔS values and discharge were compared to the observed values in the available stations. Figure 4.6 shows the comparison of the unsaturated zone ΔS and the discharge in the most downstream station in the basin which is called Son Tay station. The drainage area of this stations accounts for almost 85% of the total Red River Basin area.
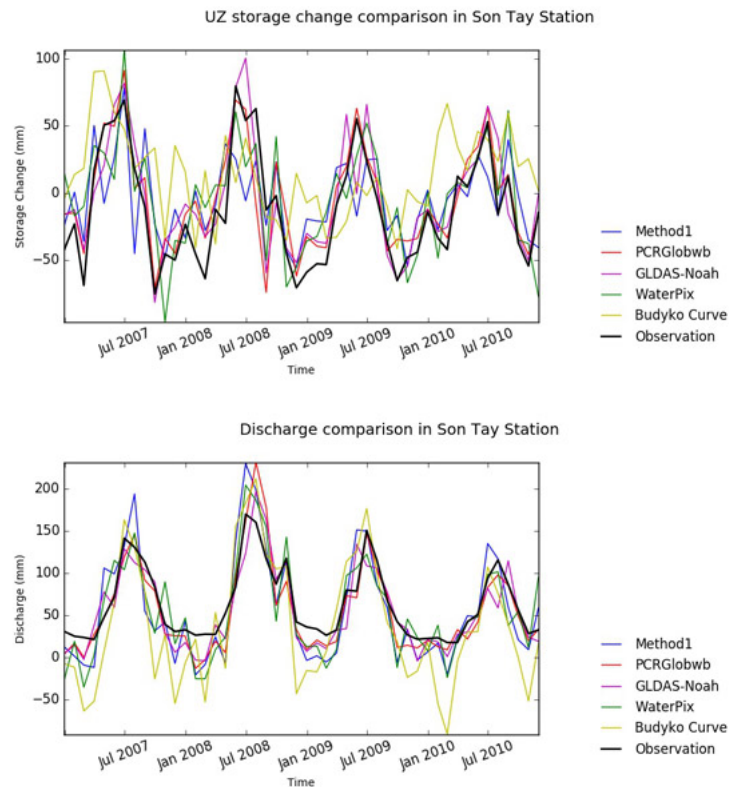
Figure 4.6: The unsaturated zone ΔS and the discharge comparison in Son Tay Station

The methods are able to produce better estimation for the discharge compared to the unsaturated zone ΔS. Moreover, the methods are able to better replicate the peaks and lows of the observed discharge in terms of timing and magnitude with an exception of July 2008, where all the methods overestimate the discharge. However, the similarities among the different methods can be better observed in the unsaturated zone ΔS comparison. The temporal dynamic of the results of both Method 1 and WaterPix are quite close to each other. However, Method 1 produces systematically lower values than WaterPix. The results from the downscaled PCRGlobwb and GLDAS-Noah are also quite similar to each other. But the downscaled PCRGlobwb are able to replicate the observed unsaturated zone ΔS more accurately compared to the downscaled GLDAS-Noah. There are some over estimation of low values during the dry period from all the 4 methods described above. The results from Budyko Curve show the least similarities to the other methods and also has the least ability to replicate both the observed unsaturated zone ΔS and the discharge.

The one on one comparison of the results from each method to the observed unsaturated zone ΔS gives a clearer impression on the performance of the different methods. Based on Figure 4.7 below and similar to what was found in Dua Station, the downscaled PCRGlobwb has the least scatter around the black 1:1 line. The most dispersion is generated from the results of the Budyko Curve method.
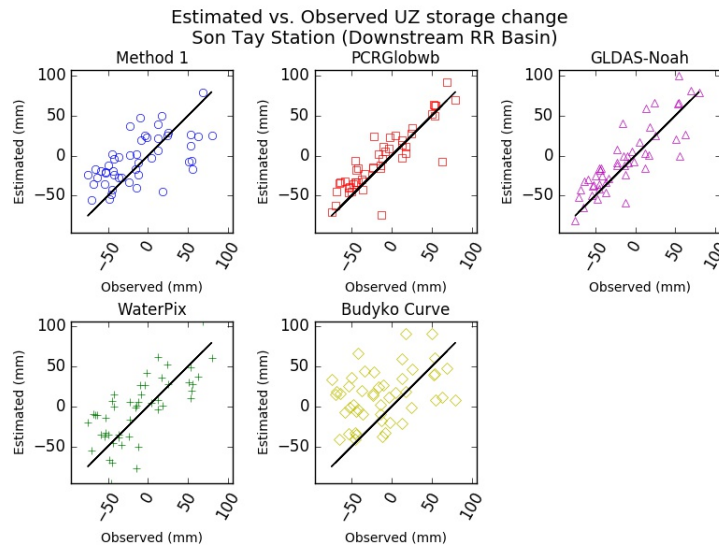
Figure 4.7: The comparison of each method to the observed unsaturated zone ΔS in the Son Tay Station
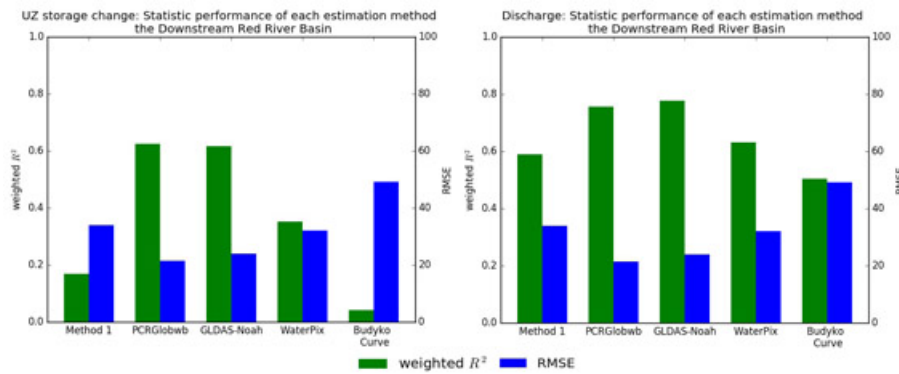
Figure 4.8: The statistical performance of the estimation methods in the Downstream Red River Basin

Using Son Tay station as the indicator, the basin-average statistical performance for the Downstream Red River Basin is shown in Figure 4.8. The downscaled PCRGlobwb and the downscaled GLDAS-Noah give similarly good performance during the unsaturated zone ΔS validation and the discharge validation. The weighted R^2 and RMSE of the downscaled PCRGlobwb during the unsaturated zone ΔS and the discharge validation are 0.62 and 21.45, and 0.75 and 21.45. The scores for the downscaled GLDAS-Noah for the same parameters are 0.62 and 23.89, and 0.78 and 23.89. On the other hand, the Budyko Curve yields the worst performance in both validations where the weighted R^2 and RMSE for the unsaturated zone ΔS are 0.04 and 49.06, and the weighted R^2 and RMSE for the discharge are 0.5 and 49.06.

4.3. Spatial Distribution Correctness

4.3.1. Ca River Basin

The three major land use and land cover classes in the Ca River Basin are the irrigated crop fields, the rain fed crop fields, and the forest group. The latter is a combination of 5 sub-classes; the secondary forest, the mangrove forest, the bamboo forest, the medium broadleaved forest, and the rich broadleaved forest. Based on the distribution of these classes in the land use and land cover map of the Ca River Basin [36], the monthly average unsaturated zone ΔS for each class can be calculated. The results are shown in Figure 4.9 below.

A clear temporal trend of the peaks and lows can be observed from the result of the STREAM model. The trend seems to coincide with the seasonal trend in Central Vietnam where May to October is considered as

the rainy season and the rest of the year as a combination of the dry season and the intermediate season. The forest class gains more water compared to the other classes on March, April, and May. However, during the rest of the rainy season, the irrigated crop field class has the more positive ΔS. The forest class has the biggest ΔS during the dry season except on February. The other method that also has a clear trend of peaks and lows is the downscaled PCRGlobwb. Similar to the STREAM model, the timing of the peaks and lows coincides with the occurrence of the rainy and the dry seasons. However, the magnitude of the monthly average ΔS differs significantly from the STREAM model. An extremely positive ΔS occurs in on August for all three classes, while the forest class has the biggest ΔS during the first three months of the rainy season and the irrigated crop field for the last two months of the same season. Same as the STREAM model, November and December are the driest month with the highest negative ΔS.

The rest of the methods do not show a coincidence between the peaks and lows trend and the seasonal trend. A more detailed breakdown of the distribution of the unsaturated zone ΔS in each land use and land class from different estimation methods is provided in Figure C.1 the Appendix section.
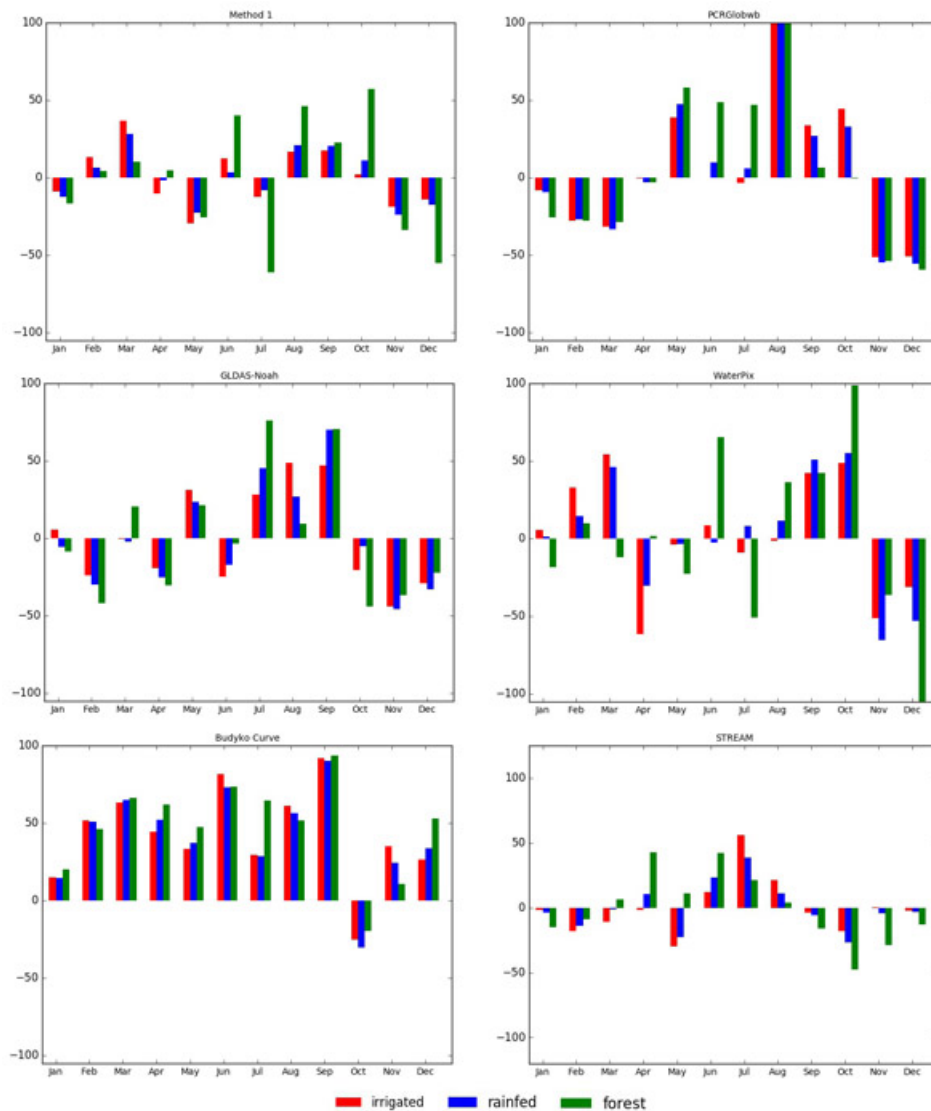
Figure 4.9: The monthly average unsaturated zone ΔS in 3 major land use and land cover classes in the Ca River Basin

4.3.2. Downstream River Basin
The forest class in the Downstream Red River Basin is an aggregation of 6 different forest sub-classes (i.e. close-open broadleaved forest, open broadleaved forest, close broadleaved forest, close needle-leaved forest,

close-open mixed forest, and permanently flooded area/forest). Based on the spatial information provided in the land use and land cover map of the Red River Basin [42], the average unsaturated zone ΔS value for the irrigated crop fields class, the rain fed crops field class, and the combined forest sub-classes were calculated. The monthly averages for each method were taken over the whole period of observation (i.e. 4 years). Figure 4.10 shows the comparison of the monthly average unsaturated zone ΔS from the different methods in the Downstream Red River Basin.
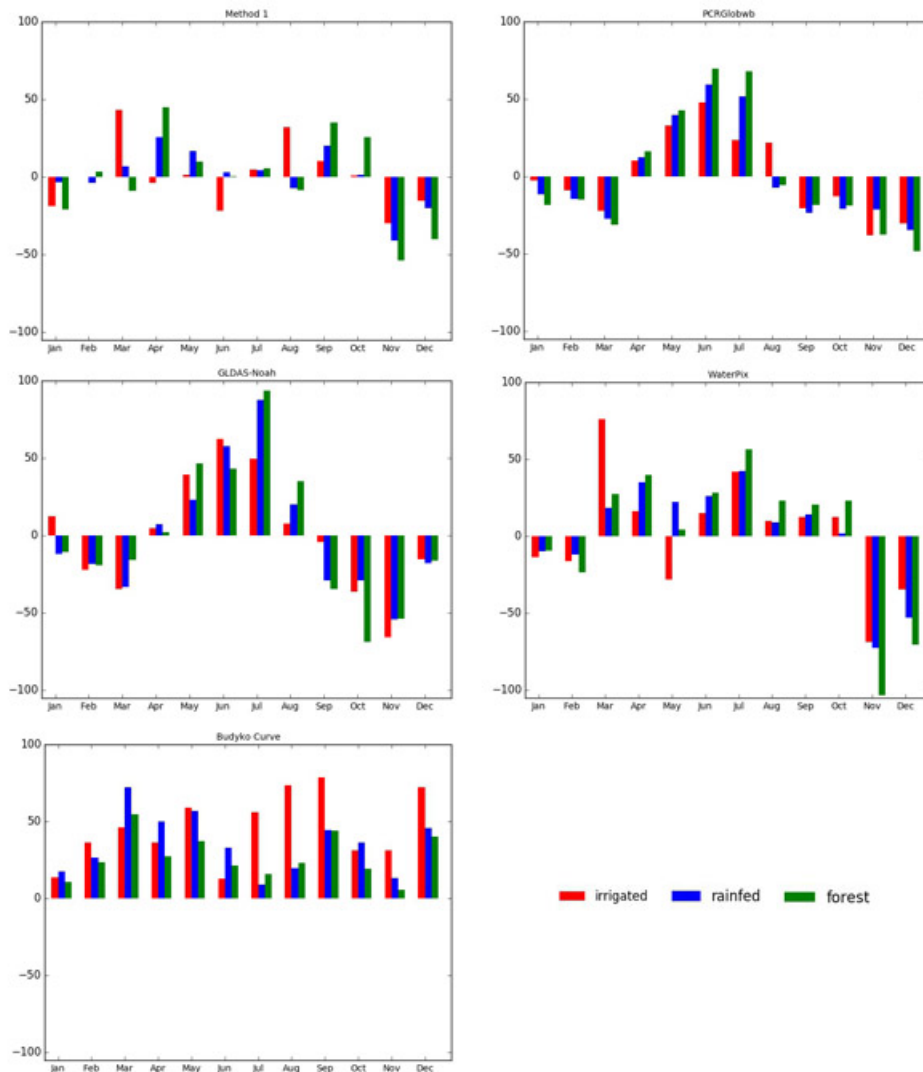
Figure 4.10: The monthly average unsaturated zone ΔS in 3 major land use and land cover classes in the Downstream Red River Basin

A clearer temporal trend of the peaks and lows can be observed from the results generated by the downscaled PCRGlobwb and the downscaled GLDAS-Noah. The timing of these peaks and lows slightly reflect the occurrence of the rainy season (i.e. around May-October) and the dry season (i.e. around November-January) in northern Vietnam. More importantly, differences between the unsaturated zone ΔS in the three major land use and land cover classes are relatively clear. During the rainy season, the forest class tends to have the highest increase in the soil moisture storage while the irrigated crop fields class has the lowest increase. However, during the dry season, the forest class is also the one that extracts the most water out of the soil storage, followed by the rain fed crop fields, and the irrigation crop fields.

The results from the other methods seem to yield different trends of peaks and lows. The empirical relationship of Method 1 generates two peaks (i.e. April and September) and one low (i.e. November). Most of the time, the forest class has higher unsaturated zone ΔS than the other classes, with the exception of March and

August. WaterPix produces two to three peaks (i.e. March, July, and October) and one low (i.e. November). The forest class has higher unsaturated zone ΔS except in January and March. The Budyko Curve yields no negative monthly average ΔS, even during the dry season. More detailed comparison between the estimated unsaturated zone ΔS in each land use and land cover class is provided in Figure C.2 the Appendix section.

5

Discussion and Recommendation

5.1. Statistical Performance of the Estimated ΔS

Both of the comparisons in the first validation approach used the same remote sensing P and actual ET products as the ones used in the calculation of WaterPix, STREAM, and the Budyko Curve method. On the other hand, PCRGlobwb and GLDAS-Noah have a completely different climate input (i.e. P and ET). The empirical relationship of Method 1 is the only one that is independent from any climatic input.

This repeating use of the same P and ET datasets as computation input might introduce a bias to the statistical performance of WaterPix, STREAM, and the Budyko Curve method. This effect is quite apparent in the STREAM model results since the model was run using the same climatic input and calibrated to the same observed streamflow data. However, the fact that WaterPix and the Budyko Curve method did not yield satisfactory performance during validation suggests that the current versions of these two methods are not suitable for the application in the Ca and the Downstream Red River Basin.

The other point of discussion is the use of a simplified monthly water balance equation to produce both the pixel-based estimated Q and the spatially-averaged unsaturated zone ΔS. In both Eq. 2.14 and Eq. 2.15, the unsaturated zone ΔS is treated as equal to the bulk term of ΔS. In other words, the water balance equation neglected the contribution of the change in surface and groundwater storage to the generation of total streamflow. In the area where the effect of both groundwater and surface storage is relatively significant, this neglect could lead to a very poor statistical agreement with the observed streamflow.

In addition to that, although the basin average performance was only evaluated at the stations with the biggest drainage area in each basin, there are smaller, upstream stations which performances should also be taken into account. More detailed explanations on each individual station are presented in the sub-sections below.

5.1.1. Individual station in the Ca River Basin

Dua station is located in the downstream part of the main Ca River. There are 2 tributaries feeding the main Ca River before the location of Dua Station; the Hieu River and the Nam Mo River. The upstream measurement of the flow in the Hieu River is available through Quy Chau Station and the downstream part is measured by Nghia Dan Station. The flow in the Nam Mo River is measured by Muong Xen Station. The performance of the estimated ΔS from the different methods were also tested in these stations. The results yielded from this test proved to be in agreement with what have been found for Dua Station validation: equally good performance of both the downscaled PCRGlobwb (i.e. weighted R^2 of 0.049, 0.071, and 0.27, and RMSE of 119.82, 94.8, and 75.83) and the downscaled GLDAS-Noah (i.e. weighted R^2 of 0.062, 0.07, and 0.09, and RMSE of 116.05, 100.31, and 83.39). A complete overview of the statistical performance of the estimation methods in the Ca River Basin can be seen in Table B.1 and Table B.2 in the Appendix section.

Apart from the 4 stations mentioned above, there are 2 other stations located in the southern part of the basin. The flow measured in these stations does not contribute to the measurement in Dua Station and their drainage areas are relatively small compared to the other sub-basins. The unsaturated zone ΔS validation was also performed for these stations. However, all the methods yield poor statistical performance where the RMSE scores are nearly twice as big as the results in the previous 4 stations and the weighted R^2s are 100 times

smaller. Therefore the results from the validation using the observation from these two stations were deemed too unreliable.

5.1.2. Individual station in the Downstream Red River Basin

Out of 6 streamflow stations that are located in the Red River Basin, only 4 of them are within the boundary of the Downstream Red River Basin. These stations measure the flow of the three main Red River tributaries. The biggest tributary is the Da River and its downstream flow is measured by Hoa Binh Station. The second biggest tributary is the Thao River and its downstream flow is measured by Yen Bai Station. Both of these tributaries originate in China. The last tributary, the Lo River, has its upstream and downstream part within the administrative boundary of Vietnam. The upstream part is measured by Bac Me Station and its downstream is measured by Vu Quang Station.

The unsaturated zone ΔS validation in these stations yields the same results as the one performed in Son Tay Station. The performance of the downscaled PCRGlobwb is found to be the best among the others, except in Yen Bai Station where the downscaled GLDAS-Noah performed slightly better than PCRGlobwb. The downscaled PCRGlobwb weighted R^2 in the stations mentioned above are 0.35, 0.65, 0.11, and 0.23 while the RMSE are 41.45, 19.08, 44.15, and 40.79. The GLDAS-Noah statistical performances for Yen Bai Station are 0.71 (weighted R^2) and 18.10 (RMSE).

Overall, the validation in Yen Bai Station yields the highest statistical parameters values for all the estimation methods and the validation in Bac Me station yields the lowest. The complete overview of the statistic scores of each estimation method in the Downstream Red River Basin can be seen in Table B.3 and Table B.4 in the Appendix section.

5.1.3. Basin average performance

Generally, the application of each estimation method in the Downstream Red River Basin yields better statistical performance compared to the application in the Ca River Basin. In addition to that, the agreement on the statistical performance of each estimation method between different sub-basins is also clearer to see in the Downstream Red River Basin.

The agreement is easily observable in Table B.3, and B.4 in the Appendix section. It can be seen that the best overall performance is given by the downscaled PCRGlobwb, followed closely by the downscaled GLDAS-Noah. The WaterPix model performance is consistently in the medium range, while the Budyko Curve method consistently underperforms the other methods. The inconclusive performance is shown by the empirical relationship of Method 1. Its RMSE values in the sub-basins are relatively better but the weighted R^2s are in the low part of the scale.

However, this division of statistical performance into groups is not that obvious in the Ca River Basin. While it is conclusive from Table B.1 and B.2 in the Appendix section that the downscaled PCRGlobwb gives the best statistical performance during the unsaturated zone ΔS validation and followed closely by the downscaled GLDAS-Noah, the performance of the rest of the methods is inconsistent.

One possibility that may explain the difference in performance between both basins is the effect of neglecting the groundwater and surface water component in the water balance equation during the validation process. It could be possible that groundwater and surface water ΔS play significant roles in the hydrological cycle of the Ca River Basin compared to the Downstream Red River Basin. The fact the Ca River Basin is half the size of the Downstream Red River Basin might also contribute to the relative importance of each hydrological fluxes and stocks.

5.2. Estimation Methods

As a model that has been calibrated specifically in Ca River Basin, it is acceptable that the STREAM model has the highest statistical performance during the discharge validation in the Ca River Basin. Unfortunately, the model is unavailable for application in the Downstream Red River.

The overall results of the validation process proved that the empirical relationship of Method 1 does not produce a reliable unsaturated zone ΔS estimation. Looking back to the computing steps in Figure 2.2 in Section 2.1, the use of a maximum rooting depth instead of an actual rooting depth could be the cause of this low performance.

The rooting depth used in this study was derived from the maximum root zone storage capacity developed by Wang-Erlandsson et al. [52]. Initially, the computation of Method 1 is done using the maximum storage capacity of 5 years return period to match the occurrence of El Nino years. However the results were not sat-

isfactory. An improvement was made when the return period for the maximum root zone storage capacity is switched to 2 years instead, considering the type of the major land cover classes and the general climatic condition. Even though the quality of the estimated unsaturated zone ΔS was improved, they are still relatively lower than the other methods. The calibration of the storage capacity in the root zone may improve the ability of Method 1 to accurately recreate the unsaturated zone ΔS.

Although the application of the Budyko Curve on unsteady and short term water balance analyses is uncommon, this study tries to use the Budyko Curve in a simplistic way to explain how the presence of ΔS will affect the water partition in monthly water balances. This is done based on the fact that, as mentioned in Section 2.4, the finite storage capacity of soil and local climate condition might influence the deviation from the asymptotes in the Budyko Curve.

However, based on the validation results, the Budyko Curve-estimated ΔS has the lowest statistical performance. An obvious explanation of this low performance is the possibility of other factors, beside the ΔS, to influence the difference between the potential and actual ET. This issue is significant, especially in areas such as the irrigated crop fields, wetlands, and permanently flooded land cover class. Further research should investigate the possible factors that, along with the ΔS, make up the difference between the potential ET and the actual ET.

The performance of WaterPix in both the Ca River Basin and the Downstream Red River Basin can be considered as medium to low. While this model still performs better than the Budyko Curve, it is too far behind the downscaled PCRGlobwb. The fact that the current version of this model does not take into account the contribution of ET from irrigation withdrawal into its monthly water balance equation could be the reason why. The effect of neglecting this withdrawal ET can be rather significant, especially in the irrigated crop field pixels. Further improvement of the model should consider adding the irrigation withdrawal to the monthly water balance.

The PCRGlobwb and GLDAS-Noah are both global models developed by reliable institutions. Huge amount of energy and efforts have been invested to improve the quality of these global models (i.e. expert knowledge to determine model parameterization, model testing, quality of forcing data, etc.). It is only logical that both models generate reliable estimation of the unsaturated zone ΔS compared to the other untested methods. The downside of using the products of these global models is the relatively coarse spatial resolution and its time-exhaustive processing nature.

5.3. The Downscaling Process

The first validation approach done in both the Ca and the Downstream Red River Basin proves that both the downscaled PCRGlobwb and GLDAS-Noah are the statistically optimal methods to estimate the unsaturated zone ΔS. However, both are global models that come with a coarse spatial resolution, which made it impractical to use in small to medium basin-scale analysis.

This study adopted a downscaling procedure developed by Agam et al. [3] and Immerzeel et al. [25] and used the monthly NDVI dataset to downscale the original PCRGlobwb and the GLDAS-Noah. By doing this, it is assumed that the spatial distribution of NDVI in the study areas represents the spatial distribution of the unsaturated zone ΔS there. In addition, since the monthly NDVI value is used to downscale both PCRGlobwb and GLDAS-Noah, it is assumed that the seasonal dynamic of the unsaturated zone storage ΔS is reflected in the changes of the monthly NDVI value. While this assumption is highly possible for the forest land cover class, it is uncommon for crop fields and other type of land cover classes.

Generally, the confidence level of the downscaled products in the Ca River Basin is higher than in the Downstream Red River Basin. Moreover, the confidence level of the downscaled GLDAS-Noah products is higher than the PCRGlobwb in the Downstream Red River Basin but lower in the Ca River Basin. The average R^2 and RMSE value for both basins are shown in Table 5.1 below.

Parameter	Ca		Downstream RR	
	PCRGlobwb	GLDAS-Noah	PCRGlobwb	GLDAS-Noah
Average Monthly R^2	0.1869	0.1708	0.1134	0.1342

Table 5.1: The confidence level of the downscaled PCRGlobwb and GLDAS-Noah in the Ca and the Downstream Red River Basin

More detailed analysis on the seasonal trend shows that, over the course of the observation period, the downscaling procedure of the PCRGlobwb products yields lower level of confidence during the rainy season

(i.e April to September) and higher level of confidence during the drier months (i.e. October to March). On the other hand, the seasonal trend of the downscaled GLDAS-Noah confidence level is a three peaks curve with March, July, and December as the best months. Lowest points are the months right after these best months. A clearer visualization of these trends is provided in Figure D.1 and Figure D.2 in the Appendix section.

The one issue that comes with this downscaling procedure is the inability of the spatially distributed correction factors to compensate for the gap between the original value and the interpolated value of the input layer. This means the average value of the disaggregated (finer-resolution) pixels does not match the value of the original (coarse-resolution) pixel. An improvement to the calculation of the correction factor so that the original coarse pixel value can be preserved is needed. This should increase the confidence level of the resulted downscaled product.

The statistical performance of the downscaled PCRGlobwb and GLDAS-Noah indicates the reliability of this downscaling procedure. In addition to that, it suggests that NDVI can be used as a proxy for the spatial distribution of soil moisture in the unsaturated zone. However, more tests in regions with different climatic and topographic characteristics are needed to conclude the reliability of this procedure. More importantly, an evaluation to see whether a downscaling procedure can actually improve the reliability of monthly soil moisture estimates from PCRGlobwb and GLDAS-Noah should be done. Both of the study areas in this study can be classified as small to medium basins, therefore the coarse pixel size of the original PCRGlobwb and GLDAS-Noah may significantly affect the basin-averaged estimate of the unsaturated zone ΔS.

5.4. Spatial Distribution Correctness

It is commonly understood that during active cropping season, the irrigated crop field land cover class will have a more negative unsaturated zone ΔS than the other land cover classes, especially the rain fed crop fields and the forest classes.

In the case of the Ca and the Downstream Red River Basin, there are 2 to 3 cropping seasons in one year. The irrigation system plays a huge role during the cropping in the dry season (i.e. October to January) while the abundance of rain during the wet summer months (i.e. May to October) reduces the dependency of the farmers to their irrigation schemes. These understandings are translated to a negative unsaturated zone ΔS during the dry season and a more positive unsaturated zone ΔS during the wet season.

The result of the land use and land cover classes distribution-based evaluation proves that the downscaled PCRGlobwb is able to reproduce the seasonal trend of the irrigated crop field land cover class. It is also found that the results of the downscaled PCRGlobwb follow the distribution of the unsaturated zone ΔS values among different land use and land cover classes as explained in the beginning of this sub-chapter, shown in Figure 5.1 below. The boxplot of other methods in both the Ca and the Downstream Red River Basin is provided in Figure C.1 and C.2 in the Appendix section.
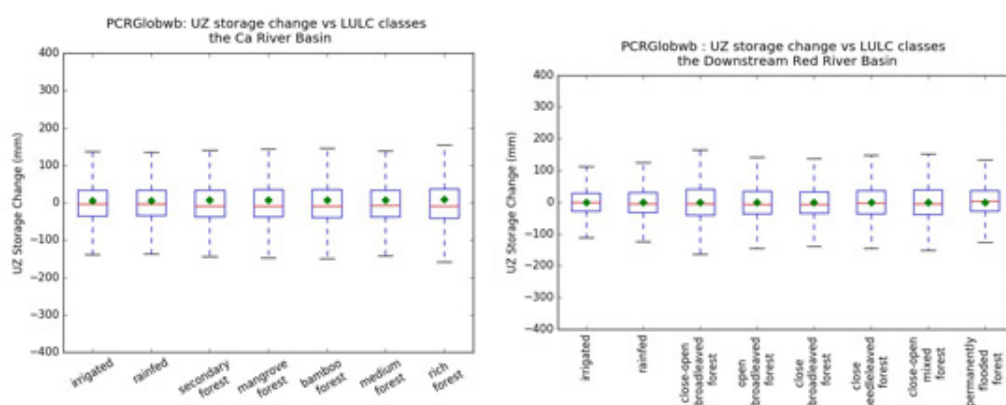

Figure 5.1: The monthly average unsaturated zone ΔS from the downscaled PRGlobwb in 3 major land use and land cover classes in the Ca River Basin and the Downscaled Red River Basin

5.5. Practical Aspect

Although the downscaled PCRGlobwb is found to be the optimum method to estimate the unsaturated zone ΔS in both study areas, it is not automatically the most suitable method for the application in the WA+ framework. As a global hydrological model, the PCRGlobwb model requires huge amount of preparation before it can be run, especially during the calibration of the model parameters. While additional expert knowledge can help to fasten the calibration process, it is still an exhaustive step that involves a big amount of computing power and time. As a consequence, this model is not calibrated most of the time.

Out of the 5 estimation methods, the empirical relationship of Method 1 can be considered as the most practical one. Its computing structure is less complicated than hydrological or land-surface models, and it is also less data intensive while still scientifically sound. The other method that shows potential is the WaterPix model. Its computing procedure requires less input data and less intensive iteration compared to the STREAM model while still preserving the elegant approach towards the streamflow generation. These characteristics will be very beneficial for an application within bigger and more complicated computing framework, such as the WA+. This is important, especially because WA+ was meant to be a friendlier water accounting method for implementation in un-gauged basins where measurement data is scarce. Other countries in the same region (e.g. Indonesia, Thailand, Malaysia, etc.) that spans over large areas require a sound water budgeting tool to improve their own water management institutions. These countries definitely can benefit from a more accurate WA+ implementation.

Acknowledging the up and growing use of the WA+ framework, the evaluation process also needs to consider the practicality and reproducibility of each of the estimation method. A more complex and data-intensive method will face more reluctance from prospective users and therefore will not be suitable for WA+ application. Ideas to improve the reliability of the empirical relationship of Method 1 and the WaterPix model should be further investigated since it will be more suitable for an implementation within the WA+ framework.

6

Conclusions

There are 4 research questions that were written in the beginning of this thesis report. These questions were constructed so that the main objective of the thesis can be achieved. The first research question asks to compare the ability of the PCRGlobwb and the GLDAS-Noah to simulate the unsaturated zone ΔS. The evaluation of the results from both models suggests that the downscaled PCRGlobwb has the better statistical performance compared to the downscaled GLDAS-Noah. Although the downscaled PCRGlobwb is slightly better than the downscaled GLDAS-Noah, both of these global models proved to be much better than the rest of the other methods.

The current version of the empirical relationship of Method 1 does not outperform either the hydrological or the land surface model. The statistical performance of Method 1 is actually rather low compared to either the hydrological or the land surface models.
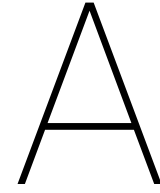
The current version WaterPix model does not take in to account the effect of irrigation withdrawal in its monthly water balance routine. This may cause a significant negative impact on its statistical performance during the validation process. However, further improvement on the computation procedure (i.e. including the ET from withdrawal) may increase its ability to generate more accurate estimates.

The Budyko Curve method yields the lowest statistical performance compared to the other methods. This can be addressed to the fact that the framework is originally meant for a long term steady water balance analysis. The ΔS does not solely explain the difference between the monthly potential and actual ET.

Reliable statistical performance from both the downscaled PCRGlobwb and GLDAS-Noah indicates that the spatial distribution of the NDVI dataset represents the spatial distribution of the unsaturated zone ΔS. Moreover, the use of monthly NDVI to downscale the monthly unsaturated zone moisture storage may help incorporate the effect of seasonality in to the models' simulation results. However, the downscaling procedure should be further investigated in regions with different hydrological characteristics to test its reliability.

The main objective of this study is to find the optimal method to estimate the unsaturated zone ΔS in order to improve the reliability of the accounting method in WA+. After evaluating 5 different estimation methods mentioned above, the final result suggests that the downscaled PCRGlobwb is able to produce statistically accurate unsaturated zone ΔS estimates. However, taking into account the methods' practicality, this global hydrological model is not the most suitable for the implementation within WA+ framework. On the other hand, the empirical relationship of Method 1 and the WaterPix model have the potential to be the optimal method although their current performances are still rather low.

A

Input for the Estimation Methods

Input	Unit	Product Description
Precipitation (P)	mm	Ca: composite products were derived from CHIRPS (Climate Hazard Group) [19] and TRMM (NASA) [29]. Downstream RR: TRMM 3B43 (NASA) [29]. Monthly time step observation was taken for both basin, from the period of January 2007 to January 2011.
Potential Total Evaporation (PET)	mm	Ca: products were obtained from the USGS SSEBop model [41] result. Donwstream RR: composite products were derived from ALEXI model, MOD16, and SSEBop model [41]. Monthly time step observation was taken for both basin, from the period of January 2007 to January 2011 [42].
Leaf Area Index (LAI)	cm^2/cm^2	Both: products were derived from NDVI datasets [26] as performed previously in the first method for the period of January 2007 to January 2011 in monthly time step.
Soil Water Index (SWI)	%	Both: ASCAT SWIT60 product the period of January 2007 to January 2011 in monthly time step [16, 34, 35, 49].
Ratio between surface runoff and baseflow (Qratio)	-	Both: products were obtained from a PCRGlobwb simulation for the period of January 2007 to January 2011 in monthly time step [22].
Number of rainy days (rainydays)	-	Both: products were derived from CHIRPS [19] for the period of January 2007 to January 2011 in monthly time step.
Max. available water content (Θ_{avail})	cm^3/cm^3	Both: products from the HiHydroSoil map courtesy of FutureWater. This is a temporally static input.
Rooting depth (h)	mm	Both: products were derived from the maximum storage capacity in the rootzone and the available water content. This is a temporally static input.

Table A.1: The list of input for the application of WaterPix Model in the Ca and the Downstream Red River Basin

Input	Product Description
Precipitation (P)	A composite product derived from CHIRPS (Climate Hazard Group) [19] and TRMM (NASA) [29] for the period of January 2007 to January 2011 in monthly time step
Potential Total Evaporation (PET)	USGS SSEBop model [41] result for the period of January 2007 to January 2011 in monthly time step.
Land Use and Land Cover (LULC)	A static land mask derived from different sources [36].
DEM	A static raster map derived from different sources [36].
Outlet locations	A text data file derived from different sources, the fill factor for the dam was set to zero to deal with constraints [36].
Calibration parameters	A text data file containing the calibrated parameter values (i.e. the Crop factor, the direct runoff-groundwater recharge separation factor, and the groundwater stock depletion factor) [36].

Table A.2: The list of input for the application of STREAM in the Ca River Basin

Input	Unit	Product Source
Max. air temperature ($t_{air,max}$)	°C	
Min. air temperature ($t_{air,min}$)	°C	
Near-surface relative humidity (q_{air})	kg/kg	GLDAS [37]
Near-surface surface pressure (p_{surf})	kPa	
Wind speed at 2 m height (wind)	m/s	
Downward short wave radiation (down_short)	W/m^2	
Downward long wave radiation (down_long)	W/m^2	CFSR [39]
Upward long wave radiation (up_long)	W/m^2	
Digital Elevation Model (DEM)	m	HydroSHED

Table A.3: The list of input for the application of Penman-Monteith reference ET formula

B

Statistical Performance Overview of the Estimation Methods

River	Sub-basin Name	Drainage Area (km^2)	Parameter	Method 1	PCRGlob wb	GLDAS-Noah	Curve Number	Budyko Curve	STREAM
Hieu	Quy Chau	1960	RMSE	149.11	119.82	116.05	170.14	142.27	117.02
			Weighted R^2	0.000057	0.049	0.062	0.000012	0.003006	0.013
	Nghia Dan	4024	RMSE	120.50	94.08	100.31	135.35	121.69	99.60
			Weighted R^2	0.00009	0.071	0.070	0.002	0.002	0.003
Nam Mo	Muong Xen	2620	RMSE	113.31	75.83	83.39	180.06	179.50	76.29
			Weighted R^2	10^{-11}	0.27	0.09	0.00013	0.10	0.02
Ca	Dua	20800	RMSE	102.02	67.84	62.79	131.26	94.69	76.31
			Weighted R^2	0.0002	0.210	0.174	0.002	0.029	0.006
Ngan Sau	Hoa Duyet	1880	RMSE	231.57	237.57	268.75	262.25	234.35	220.01
			Weighted R^2	0.0001	0.0001	0.0003	0.003	0.011	0.002
Ngan Pho	Son Diem	790	RMSE	208.90	170.37	198.28	229.23	181.18	173.46
			Weighted R^2	0.000043	0.026	0.00005	0.000193	0.030	0.007

Table B.1: The overview of statistical performance of the unsaturated zone ΔS estimation in the Ca River Basin

River	Sub-basin Name	Drainage Area (km^2)	Parameter	Method 1	PCRGlobwb	GLDAS-Noah	Curve Number	Budyko Curve	STREAM
Hieu	Quy Chau	1960	RMSE	149.11	119.80	115.83	170.17	142.27	117.02
			Weighted R^2	0.02	0.12	0.10	0.01	0.12	0.21
	Nghia Dan	4024	RMSE	120.50	94.08	100.31	135.35	121.69	99.60
			Weighted R^2	0.06	0.21	0.18	0.06	0.24	0.36
Nam Mo	Muong Xen	2620	RMSE	113.31	75.59	83.13	180.03	179.52	76.29
			Weighted R^2	0.14	0.31	0.29	0.01	0.23	0.33
Ca	Dua	20800	RMSE	102.02	67.84	62.79	131.26	94.69	76.31
			Weighted R^2	0.02	0.26	0.30	0.0002	0.24	0.27
Ngan Sau	Hoa Duyet	1880	RMSE	231.57	237.61	268.74	262.11	234.35	219.92
			Weighted R^2	0.28	0.26	0.15	0.19	0.37	0.34
Ngan Pho	Son Diem	790	RMSE	181.18	170.37	198.30	228.94	181.18	173.47
			Weighted R^2	0.15	0.26	0.15	0.13	0.35	0.31

Table B.2: The overview of statistical performance of the discharge estimation in the Ca River Basin

River	Sub-basin Name	Drainage Area (km^2)	Parameter	Method 1	PCRGlobwb	GLDAS-Noah	Curve Number	Budyko Curve
Da	Hoa Binh	50880.41	RMSE	44.58	41.45	46.72	48.42	58.40
			Weighted R^2	0.16	0.35	0.23	0.16	0.09
Thao	Yen Bai	48833.26	RMSE	25.42	19.08	18.10	23.85	28.58
			Weighted R^2	0.42	0.65	0.71	0.48	0.26
Lo	Bac Me	9266.41	RMSE	53.25	44.15	59.34	60.54	75.65
			Weighted R^2	0.00002	0.11	0.009	0.0052	0.00013
	Vu Quang	31218.68	RMSE	60.31	40.79	54.25	63.59	78.87
			Weighted R^2	0.00140	0.23	0.09	0.04	0.00001
Red River	Son Tay	137861.98	RMSE	33.87	21.45	23.89	32.08	49.06
			Weighted R^2	0.17	0.62	0.62	0.35	0.04

Table B.3: The overview of statistical performance of the unsaturated zone ΔS estimation in the Downstream Red River Basin

River	Sub-basin Name	Drainage Area (km^2)	Parameter	Method 1	PCRGlobwb	GLDAS-Noah	Curve Number	Budyko Curve
Da	Hoa Binh	50880.41	RMSE	44.58	41.10	46.72	48.42	58.40
			Weighted R^2	0.64	0.58	0.47	0.48	0.69
Thao	Yen Bai	48833.26	RMSE	25.42	19.08	18.10	23.85	28.58
			Weighted R^2	0.57	0.67	0.70	0.59	0.50
Lo	Bac Me	9266.41	RMSE	53.25	44.15	59.34	60.54	75.65
			Weighted R^2	0.38	0.34	0.12	0.23	0.49
	Vu Quang	31218.68	RMSE	60.31	40.79	54.25	63.59	78.87
			Weighted R^2	0.48	0.55	0.24	0.33	0.43
Red River	Son Tay	137861.98	RMSE	33.87	21.45	23.89	32.08	49.06
			Weighted R^2	0.59	0.75	0.78	0.63	0.50

Table B.4: The overview of statistical performance of the discharge estimation in the Downstream Red River Basin

C

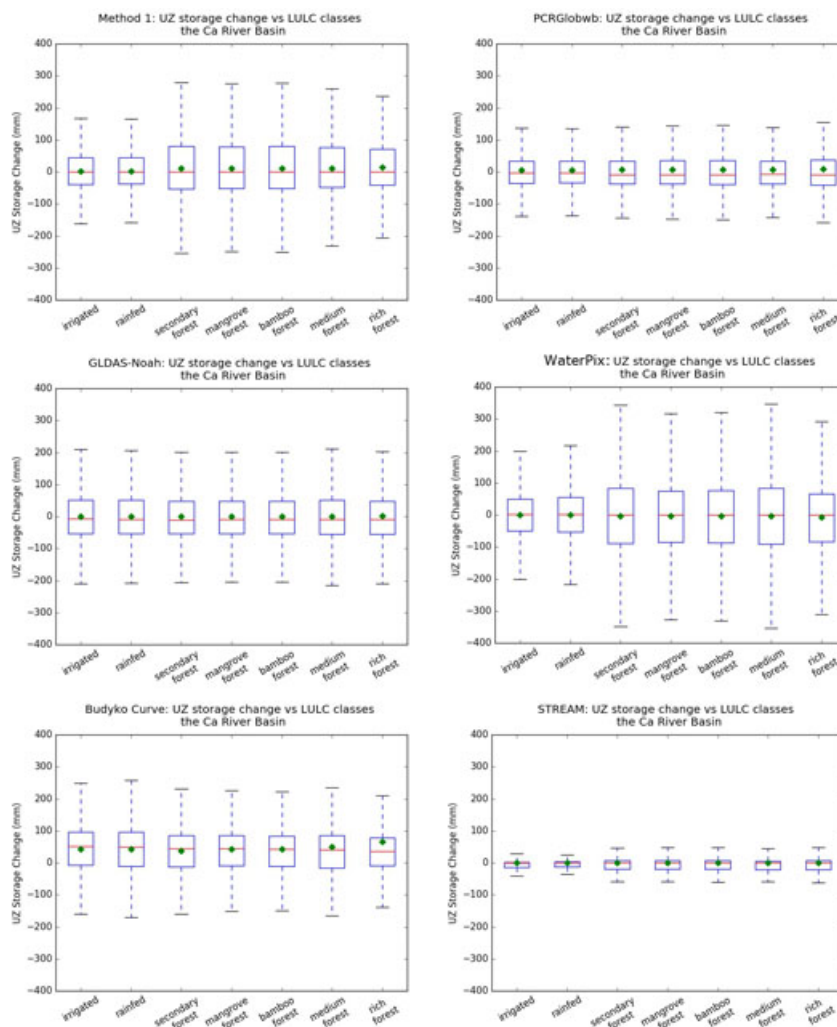# The Land Use and Land Cover Based Evaluation

Figure C.1: The monthly average unsaturated zone ΔS in 3 major land use and land cover classes in the Ca River Basin
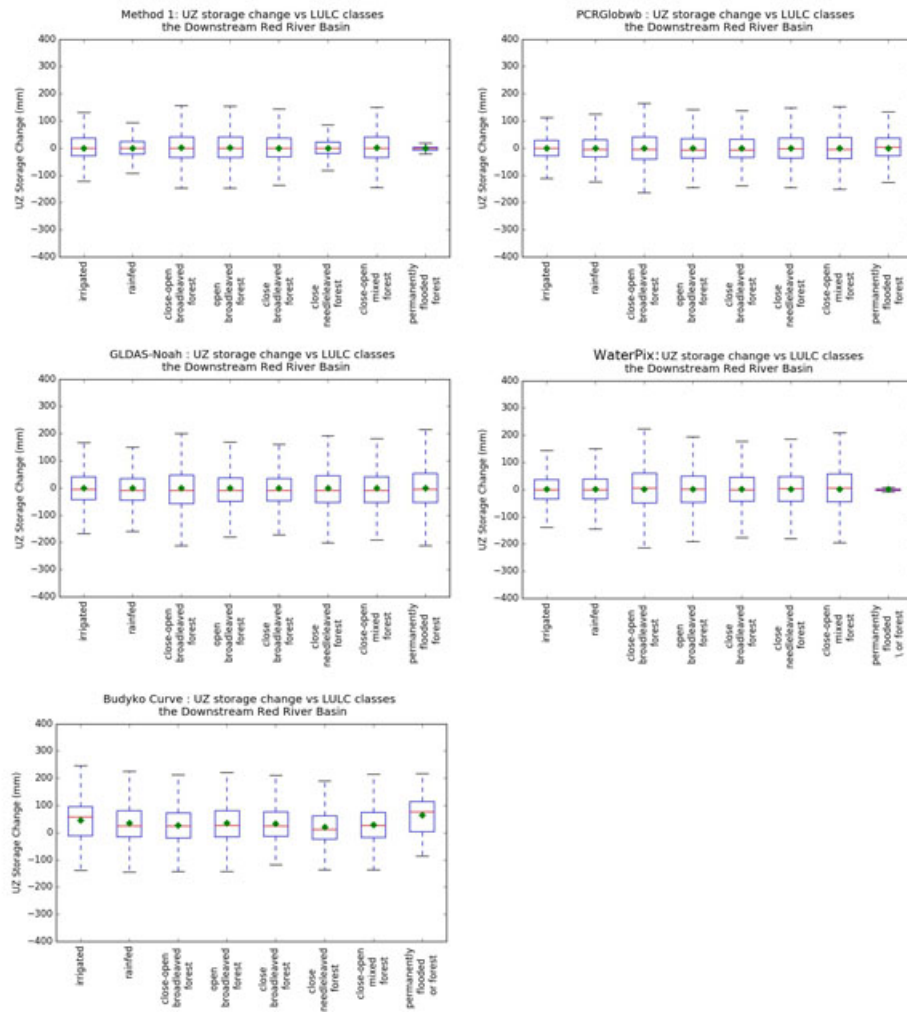
Figure C.2: The unsaturated zone ΔS in 3 major land use and land cover classes in the Downstream Red River Basin

D

Evaluation of the Downscaling Process

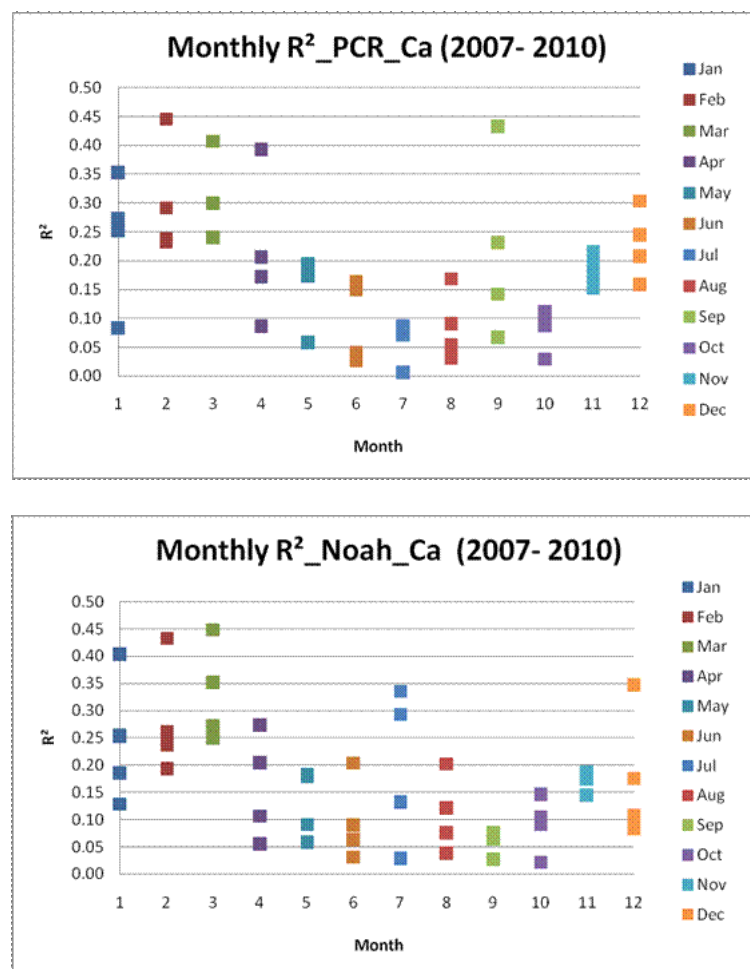Figure D.1: The monthly R^2 of the downscaled PCRGlobwb and GLDAS-Noah products in the Ca River Basin
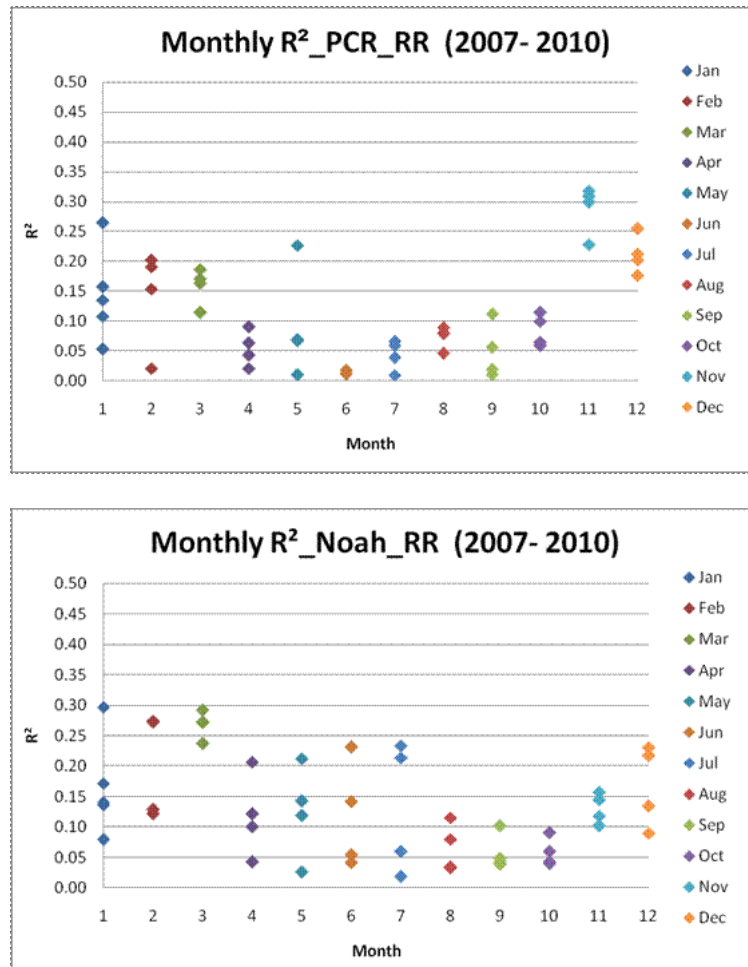
Figure D.2: The monthly R^2 of the downscaled PCRGlobwb and GLDAS-Noah products in the Downstream Red River Basin

Bibliography

[1] *A Hydro-meteorological Flood Forecasting System For The Red and Ca Rivers (China, Laos, and Vietnam) Part I – Investigated Areas and Model Setup*, 2012.

[2] J.C.J.H. Aerts, M. Kriek, and M. Schepel. STREAM (Spatial tools for river basins and environment and analysis of management options): 'set up and requirements'. *Physics and Chemistry of the Earth, Part B: Hydrology, Oceans and Atmosphere*, 24:591–595, 1999. doi: doi:10.1016/S1464-1909(99)00049-0.

[3] N. Agam, W.P. Kustas, M.C. Anderson, F. Li, and P.D. Colaizzi. Utility of thermal sharpening over Texas high plains irrigated agricultural fields. *Journal of Geophysical Research: Atmospheres*, 112(D19), 2007. ISSN 2156-2202. doi: 10.1029/2007JD008407. URL http://dx.doi.org/10.1029/2007JD008407.

[4] R.G. Allen, L.S. Pereira, D.R. Raes, and M. Smith. *Crop evapotranspiration – Guidelines for computing crop water requirements – FAO Irrigation and drainage paper 56*, 1998.

[5] W.G.M. Bastiaanssen, M. Menenti, R.A. Feddes, and A.A.M. Holtslag. A remote sensing surface energy balance algorithm for land (SEBAL). 1. Formulation. *Journal of Hydrology*, 212–213:198–212, 1998. ISSN 0022-1694. doi: http://dx.doi.org/10.1016/S0022-1694(98)00253-4. URL http://www.sciencedirect.com/science/article/pii/S0022169498002534.

[6] W.G.M. Bastiaanssen, M.J.M. Cheema, W.W. Immerzeel, I.J. Miltenburg, and H. Pelgrum. Surface energy balance and actual evapotranspiration of the transboundary Indus Basin estimated from satellite measurements and the ETLook model. *Water Resources Research*, 48(11), 2012. ISSN 1944-7973. doi: 10.1029/2011WR010482. URL http://dx.doi.org/10.1029/2011WR010482.

[7] H. Bi, J. Ma, W. Zheng, and J. Zeng. Comparison of soil moisture in GLDAS model simulations and in situ observations over the Tibetan Plateau. *Journal of Geophysical Research: Atmospheres*, 121(6): 2658–2678, 2016. ISSN 2169-8996. doi: 10.1002/2015JD024131. URL http://dx.doi.org/10.1002/2015JD024131.

[8] A. Castelletti, F. Pianosi, X. Quach, and R. Soncini-Sessa. Assessing water reservoirs management and development in Northern Vietnam. *Hydrology and Earth System Sciences*, 16(1):189–199, 2012. doi: 10.5194/hess-16-189-2012. URL http://www.hydrol-earth-syst-sci.net/16/189/2012/.

[9] T. de Boer-Euser, H.K. McMillan, M. Hrachowitz, H.C. Winsemius, and H.H.G. Savenije. Influence of soil and climate on root zone storage capacity. *Water Resources Research*, 52(3):2009–2024, 2016. ISSN 1944-7973. doi: 10.1002/2015WR018115. URL http://dx.doi.org/10.1002/2015WR018115.

[10] N.V. Diep, N.H. Khanh, N.M. Son, N.V. Hanh, and P. Huntjens. Integrated Water Resource Management in the Red River Basin – Problems and Cooperation Opportunity.

[11] Conservation Engineering Division. Urban Hydrology for Small Watersheds. Technical Release 55, Natural Resources Conservation Services, United States Department of Agriculture (USDA), June 1986.

[12] United Nation Statistics Division. *UN: System of Environmental Economic Accounting for Water*. United Nation.

[13] R. J. Donohue, M. L. Roderick, and T. R. McVicar. On the importance of including vegetation dynamics in Budyko's hydrological model. *Hydrology and Earth System Sciences*, 11(2):983–995, 2007. doi: 10.5194/hess-11-983-2007. URL http://www.hydrol-earth-syst-sci.net/11/983/2007/.

[14] M.B. Ek, K.E. Mitchell, Y. Lin, E. Rogers, P. Grunmann, V. Koren, G. Gayno, and J.D. Tarpley. Implementation of Noah land surface model advances in the National Centers for Environmental Prediction operational mesoscale ETa model. *Journal of Geophysical Research: Atmospheres*, 108(D22), 2003. ISSN 2156-2202. doi: 10.1029/2002JD003296. URL http://dx.doi.org/10.1029/2002JD003296.

[15] G.E Espinoza-Dávalos and W.G.M. Bastiaanssen. WaterPix Model: Estimation of Runoff from Pixel-Scale Water Balances. 2016. URL https://github.com/wateraccounting.

[16] EUMETSAT. EUMETSAT-HSAF Metop ASCAT Soil Moisture, WARPS5.5R2.2, HSAF product H25-SM-OBS-4. URL http://hsaf.meteoam.it. provided daily as global maps of 5-day composite or mean separately for descending and ascending Metop overpasses.

[17] GFDRR (Global Facility for Disaster Reduction and Recovery). Climate Risk and Adaptation Country Profile: Vulnerability, Risk Reduction, and Adaptation to Climate Change in Vietnam, April 2011.

[18] The UNESCO-IHP Regional Steering Committee for Southeast Asia and The Pacific. Catalogue of Rivers For Southeast Asia and The Pacific Volume vi, 2012.

[19] C. Funk, P. Peterson, M. Landsfeld, D. Pedreros, J. Verdin, S. Shukla, G. Husak, J. Rowland, L. Harrison, A. Hoell, and J. Michaelsen. The climate hazards infrared precipitation with stations—a new environmental record for monitoring extremes. *Scientific Data*, 2, 2015. doi: 10.1038/sdata.2015.66. URL http://dx.doi.org/10.1038/sdata.2015.66.

[20] H. Gao, M. Hrachowitz, S.J. Schymanski, F. Fenicia, N. Sriwongsitanon, and H.H.G. Savenije. Climate controls how ecosystems size the root zone storage capacity at catchment scale. *Geophysical Research Letters*, 41(22):7916–7923, 2014. ISSN 1944-8007. doi: 10.1002/2014GL061668. URL http://dx.doi.org/10.1002/2014GL061668.

[21] E.P. Glenn, A.R. Huete, P.L. Nagler, and S.G. Nelson. Relationship Between Remotely-sensed Vegetation Indices, Canopy Attributes and Plant Physiological Processes: What Vegetation Indices Can and Cannot Tell Us About the Landscape. *Sensors*, 8(4):2136, 2008. ISSN 1424-8220. doi: 10.3390/s8042136. URL http://www.mdpi.com/1424-8220/8/4/2136.

[22] S. Hagemann and L.D. Gates. Improving a subgrid runoff parameterization scheme for climate models by the use of high resolution data derived from satellite observations. *Climate Dynamics*, 21(3): 349—359, 2003. ISSN 1432-0894. doi: 10.1007/s00382-003-0349-x. URL http://dx.doi.org/10.1007/s00382-003-0349-x.

[23] T.S. Hogue, L. Bastidas, H. Gupta, S. Sorooshian, K. Mitchell, and W. Emmerich. Evaluation and transferability of the Noah land surface model in semiarid environments. *Journal of Hydrometeorology*, 6(1): 68——84, February 2005. ISSN 1525-755X. doi: 10.1175/JHM-402.1.

[24] R.T.W.L. Hurkmans, H. de Moel, J.C.J.H. Aerts, and P.A. Troch. Water balance versus land surface model in the simulation of Rhine river discharges. *Water Resources Research*, 44(1), 2008. ISSN 1944-7973. doi: 10.1029/2007WR006168. URL http://dx.doi.org/10.1029/2007WR006168.

[25] W. W. Immerzeel, M.M. Rutten, and P. Droogers. Spatial downscaling of TRMM precipitation using vegetative response on the Iberian Peninsula. *Remote Sensing of Environment*, 113(2):362–370, 2009. ISSN 0034-4257. doi: http://dx.doi.org/10.1016/j.rse.2008.10.004. URL http://www.sciencedirect.com/science/article/pii/S0034425708003155.

[26] C.B. Jenkerson, T. Maiersperger, and G. Schmidt. eMODIS: A user-friendly data source: U.S. Geological Survey Open-File Report 2010–1055. Technical report, USGS, 2010.

[27] P. Karimi, W. G. M. Bastiaanssen, and D. Molden. Water Accounting Plus (WA+) a water accounting procedure for complex river basins based on satellite measurements. *Hydrology and Earth System Sciences*, 17 (7):2459–2472, 2013. doi: 10.5194/hess-17-2459-2013. URL http://www.hydrol-earth-syst-sci.net/17/2459/2013/.

[28] P. Krause, D. P. Boyle, and F. Base. Comparison of different efficiency criteria for hydrological model assessment. *Advances in Geosciences*, 5:89–97, 2005. doi: 10.5194/adgeo-5-89-2005. URL http://www.adv-geosci.net/5/89/2005/.

[29] C. Kummerow, W. Barnes, T. Kozu, J. Shiue, and J. Simpson. The Tropical Rainfall Measuring Mission (TRMM) Sensor Package. *Journal of Atmospheric and Oceanic Technology*, 15(3):809–817, 1998. doi: 10.1175/1520-0426(1998)015<0809:TTRMMT>2.0.CO;2. URL http://dx.doi.org/10.1175/15200426(1998)015<0809:TTRMMT>2.0.CO;2.

[30] C. McSweeney, M. New, and G. Lizcano. UNDP Climate Change Country Profiles: Vietnam.

[31] C. Michel, V. Andréassian, and C. Perrin. Soil Conservation Service Curve Number method: How to mend a wrong soil moisture accounting procedure? *Water Resources Research*, 41(2), 2005. ISSN 1944-7973. doi: 10.1029/2004WR003191. URL http://dx.doi.org/10.1029/2004WR003191.

[32] P.C.D. Milly. Climate, soil water storage, and the average annual water balance. *Water Resources Research*, 30(7):2143–2156, 1994. ISSN 1944-7973. doi: 10.1029/94WR00586. URL http://dx.doi.org/10.1029/94WR00586.

[33] K. Mitchell. *The Community Noah Land-Surface Model (LSM): User Guide Public Release Version 2.7.1*. National Center for Atmospheric Research, February 2005.

[34] V. Naeimi, C. Paulik, A. Bartsch, W. Wagner, R. Kidd, S.E. Park, K. Elger, and J. Boike. ASCAT Surface State Flag (SSF): Extracting Information on Surface Freeze/Thaw Conditions From Backscatter Data Using an Empirical Threshold-Analysis Algorithm, year =. *IEEE Transactions on Geoscience and Remote Sensing*.

[35] V. Naeimi, K. Scipal, Z. Bartalis, S. Hasenauer, and W. Wagner. An Improved Soil Moisture Retrieval Algorithm for ERS and METOP Scatterometer Observations. *IEEE Transactions on Geoscience and Remote Sensing*, 47(7):1999–2013, July 2009. ISSN 0196-2892. doi: 10.1109/TGRS.2008.2011617.

[36] A. Poortinga, W. Bastiaanssen, G. Simons, D. Saah, G. Senay, M. Fenn, B. Bean, and J. Kadyszewski. A new self-calibrating high resolution runoff and streamflow remote sensing model for ungauged basins using open access earth observation data sets. An ongoing project between Winrock International, TU Delft, UNESCO-IHE, FutureWater, USGS, University of San Francisco, and Spatial Informatics Group., 2016.

[37] M. Rodell and H.K. Beaudoing. GLDAS Noah Land Surface Model L4 3 hourly 0.25 x 0.25 degree.

[38] M. Rodell, P.R. Houser, U. Jambor, J. Gottschalck, K. Mitchell, C-J. Meng, K. Arsenault, B. Cosgrove, J. Radakovich, M. Bosilovich, J.K. Entin*, J.P. Walker, D. Lohmann, and D. Toll. The Global Land Data Assimilation System. *Bulletin of the American Meteorological Society*, 85(3):381–394, 2004. doi: 10.1175/BAMS-85-3-381. URL http://dx.doi.org/10.1175/BAMS-85-3-381.

[39] S. Saha, S. Moorthi, H. L. Pan, X. Wu, J. Wang, S. Nadiga, P. Tripp, R. Kistler, J. Woollen, D. Behringer, H. Liu, D. Stokes, R. Grumbine, G. Gayno, J. Wang, Y. T. Hou, H. Y. Chuang, H. M. H. Juang, J. Sela, M. Iredell, R. Treadon, D. Kleist, P. Van Delst, D. Keyser, J. Derber, M. Ek, J. Meng, H. Wei, R. Yang, S. Lord, H. van den Dool, A. Kumar, W. Wang, C. Long, M. Chelliah, Y. Xue, B. Huang, J. K. Schemm, W. Ebisuzaki, R. Lin, P. Xie, M. Chen, S. Zhou, W. Higgins, C. Z. Zou, Q. Liu, Y. Chen, Y. Han, L. Cucurull, R. W. Reynolds, G. Rutledge, and M. Goldberg. NCEP Climate Forecast System Reanalysis (CFSR) Selected Hourly Time-Series Products, January 1979 to December 2010, 2010. URL http://dx.doi.org/10.5065/D6513W89.

[40] H.H.G. Savenije. Lecture notes of Hydrological Modelling, January 2009.

[41] G.B. Senay, S. Bohms, R.K. Singh, P.H. Gowda, N.M. Velpuri, H. Alemu, and J.P. Verdin. Operational Evapotranspiration Mapping Using Remote Sensing and Weather Datasets: A New Parameterization for the SSEB Approach. *JAWRA Journal of the American Water Resources Association*, 49(3):577–591, 2013. ISSN 1752-1688. doi: 10.1111/jawr.12057. URL http://dx.doi.org/10.1111/jawr.12057.

[42] G. Simons, W. Bastiaanssen, L.A. Ngô, C.R. Hain, M. Anderson, and G. Senay. Integrating Global Satellite-Derived Data Products as a Pre-Analysis for Hydrological Modelling Studies: A case study for the Red River Basin. *Remote Sensing*, 8(4), 2016. ISSN 2072-4292. doi: 10.3390/rs8040279. URL http://www.mdpi.com/2072-4292/8/4/279.

[43] M. Sivapalan, K. Takeuchi, S.W. Franks, V.K. Gupta, H. Karambiri, V. Lakshmi, X. Liang, J.J. McDonnell, E.M. Mendiondo, P.E. O'Connell, T. Oki, J.W. Pomeroy, T. Schertzer, S. Uhlenbrook, and E. Zehe. IAHS Decade on Predictions in Ungauged Basins (PUB), 2003–2012: Shaping an exciting future for the hydrological sciences. *Hydrological Sciences Journal*, 48(6):857–880, 2003. doi: 10.1623/hysj.48.6.857.51421. URL http://dx.doi.org/10.1623/hysj.48.6.857.51421.

[44] J. Soussan and L. Linde. Strategic Environmental Assessment and the Calculation of Ecosystem Services Values in the Red River Basin in Vietnam. Technical report, September 2013.

[45] L.P.H. Van Beek and M.F.P. Bierkens. The Global Hydrological Model PCR-GLOBWB: Conceptualization, Parameterization, and Verification. Technical report, Department of Physical Geography, Utrecht University, Utrecht, The Netherlands, 2008. URL http://vanbeek.geo.uu.nl/suppinfo/vanbeekbierkens2009.pdf.

[46] L.P.H. van Beek, Y. Wada, and M.F.P. Bierkens. Global monthly water stress: 1. water balance and water availability. *Water Resources Research*, 47(7), 2011. ISSN 1944-7973. doi: 10.1029/2010WR009791. URL http://dx.doi.org/10.1029/2010WR009791.

[47] N.D. Viet. Trade-offs between water supply and health of the Red River in Vietnam, March 2016. URL http://vawr-mk33.com/blogs/trade-offs-between-the-water-supply-and-healthy-of-red-river-in-vietnam/.

[48] Y. Wada, D. Wisser, and M.F.P. Bierkens. Global modeling of withdrawal, allocation and consumptive use of surface water and groundwater resources. *Earth System Dynamics*, 5(1):15–40, 2014. doi: 10.5194/esd-5-15-2014. URL http://www.earth-syst-dynam.net/5/15/2014/.

[49] W. Wagner, G. Lemoine, and H. Rott. A method for estimating soil moisture from {ERS} scatterometer and soil data. *Remote Sensing of Environment*, 70(2):191–207, 1999. ISSN 0034-4257. doi: http://dx.doi.org/10.1016/S0034-4257(99)00036-X. URL http://www.sciencedirect.com/science/article/pii/S003442579900036X.

[50] D. Wang. Evaluating interannual water storage changes at watersheds in Illinois based on long-term soil moisture and groundwater level data. *Water Resources Research*, 48(3), 2012. ISSN 1944-7973. doi: 10.1029/2011WR010759. URL http://dx.doi.org/10.1029/2011WR010759.

[51] D. Wang and N. Alimohammadi. Responses of annual runoff, evaporation, and storage change to climate variability at the watershed scale. *Water Resources Research*, 48(5), 2012. ISSN 1944-7973. doi: 10.1029/2011WR011444. URL http://dx.doi.org/10.1029/2011WR011444.

[52] L. Wang-Erlandsson, W.G.M. Bastiaanssen, H. Gao, J. Jägermeyr, G.B. Senay, A.I.J.M. vanÂ Dijk, J.P. Guerschman, P.W. Keys, L.J. Gordon, and H.H.G. Savenije. Global root zone storage capacity from satellite-based evaporation. *Hydrology and Earth System Sciences*, 20(4):1459–1481, 2016. doi: 10.5194/hess-20-1459-2016. URL http://www.hydrol-earth-syst-sci.net/20/1459/2016/.

[53] C. A. Williams, M. Reichstein, N. Buchmann, D. Baldocchi, C. Beer, C. Schwalm, G. Wohlfahrt, N. Hasler, C. Bernhofer, T. Foken, D. Papale, S. Schymanski, and K. Schaefer. Climate and vegetation controls on the surface water balance: Synthesis of evapotranspiration measured across a global network of flux towers. *Water Resources Research*, 48(6), 2012. ISSN 1944-7973. doi: 10.1029/2011WR011586. URL http://dx.doi.org/10.1029/2011WR011586. W06523.

[54] H.C. Winsemius, H.H.G. Savenije, A.M.J. Gerrits, E.A. Zapreeva, and R. Klees. Comparison of two model approaches in the zambezi river basin with regard to model reliability and identifiability. *Hydrology and Earth System Sciences*, 10(3):339–352, 2006. doi: 10.5194/hess-10-339-2006. URL http://www.hydrol-earth-syst-sci.net/10/339/2006/.